Double-Slope Solar Still Productivity Based on the Number of Rubber Scraper Motions

Ali O. Al-Sulttani [1], **Amimul Ahsan** [2,3], **Basim A. R. Al-Bakri** [4], **Mahir Mahmod Hason** [5], **Nik Norsyahariati Nik Daud** [6], **S. Idrus** [6], **Omer A. Alawi** [7], **Elżbieta Macioszek** [8,*] and **Zaher Mundher Yaseen** [9,*]

1 Department of Water Resources Engineering, University of Baghdad, Baghdad 10071, Iraq
2 Department of Civil and Environmental Engineering, Islamic University of Technology (IUT), Gazipur 1704, Bangladesh
3 Department of Civil and Construction Engineering, Swinburne University of Technology, Melbourne, VIC 3000, Australia
4 Department of Aeronautical Engineering, University of Baghdad, Baghdad 10071, Iraq
5 Disaster Information Management Centre, Ministry of Science and Technology, Baghdad 10071, Iraq
6 Department of Civil Engineering, Faculty of Engineering, Universiti Putra Malaysia, Serdang 43400, Selangor, Malaysia
7 Department of Thermofluids, School of Mechanical Engineering, Universiti Teknologi Malaysia, Skudai 81310, Johor Bahru, Malaysia
8 Department of Transport Systems, Traffic Engineering and Logistics, Faculty of Transport and Aviation Engineering, Silesian University of Technology, Krasińskiego 8 Street, 40-019 Katowice, Poland
9 Civil and Environmental Engineering Department, King Fahd University of Petroleum & Minerals, Dhahran 31261, Saudi Arabia
* Correspondence: elzbieta.macioszek@polsl.pl (E.M.); z.yaseen@kfupm.edu.sa (Z.M.Y.)

Abstract: In low-latitude areas less than $10°$ in latitude angle, the solar radiation that goes into the solar still increases as the cover slope approaches the latitude angle. However, the amount of water that is condensed and then falls toward the solar-still basin is also increased in this case. Consequently, the solar yield still is significantly decreased, and the accuracy of the prediction method is affected. This reduction in the yield and the accuracy of the prediction method is inversely proportional to the time in which the condensed water stays on the inner side of the condensing cover without collection because more drops will fall down into the basin of the solar-still. Different numbers of scraper motions per hour (*NSM*), that is, 1, 2, 3, 4, 5, 6, and 7, are implemented to increase the hourly yield of solar still (HYSS) of the double-slope solar still hybrid with rubber scrapers (DSSSHS) in areas at low latitudes and develop an accurate model for forecasting the HYSS. The proposed model is developed by determining the best values of the constant factors that are associated with *NSM*, and the optimal values of exponent (*n*) and the unknown constant (*C*) for the Nusselt number expression (*Nu*). These variables are used in formulating the models for estimating HYSS. The particle swarm optimization (PSO) algorithm is used to solve the optimization problem, thereby determining the optimal yields. Water that condensed and accumulated inside the condensing glass cover of the DSSSHS is collected by increasing *NSM*. This process increases in the specific productivity of DSSSHS and the accuracy of the HYSS prediction model. Results show that the proposed model can consistently and accurately estimate HYSS. Based on the relative root mean square error (*RRMSE*), the proposed model PSO–HYSS attained a minimum value (2.81), whereas the validation models attained Dunkle's (78.68) and Kumar and Tiwari's (141.37).

Keywords: specific productivity; rubber scraper motions; solar still; particle swarm optimization

1. Introduction

1.1. Research Background

Potable water is vital for our existence. More than 75 percent of the globe is covered by water, but only 0.014 percent of it is potable. Meanwhile, the demand for potable water is continuously increasing with population, high living standards, and expansion of industrial and agricultural activities [1]. Therefore, affordable, safe, sustainable, and environmentally friendly methods for producing potable water from saltwater must be developed. These techniques include the solar–distillation technique, which is a favorable technique that distills salty water using solar energy; this technique is safe for the environment as it operates using only sustainable energy [2]. This technology can resolve the shortage of potable water, particularly in remote, rugged, arid, and coastal areas, without damaging the environment; however, it is still doubted because it produces only a small amount of potable water [3]. Thus, the productivity of solar distillation technology is a prime challenge that needs modifications in operation and design for its improvement.

1.2. Adopted Literature

With the goal of enhancing the productivity of solar stills, this work tests them using different designs and techniques, namely double-glass glaze between which brine flows [4], water and air flows [5], drum solar still with reflectors, integrated with solar dishes [6], sponge cubes in the solar still basin of various sizes [7], an elevated basin solar still with integrated internal reflectors and inclined fins [8], solar still coupled with evacuated tube solar collector [9], built-in reservoir for sand heat [10], using parabolic dish collector [11], increased condensation area [12], geothermal energy [13], augmented with sand-filled cotton bags [14], parabolic concentrator with heat exchanger and focal pipe [15], added aluminum balls inside the solar distillate box [16], solar collector with water sprinkler and thermoelectric cooler [17,18], triangular and tubular solar stills [19,20], fin at the basin of the still [21], parabolic concentrator tubular solar stills [22,23], inside and outside reflectors [24], tubular vinyl chloride sheet with transparent polythene film covers [25], thermoelectric cooler [26], cost-saving techniques [27], forced convection within solar still [28], size partition and optimized location within a single-slope solar still [29], nanomaterials with and without a vacuum fan [30]. On the other hand, improving the productivity of single effect double-slope solar still by modification simple [31], incorporating a double-slope solar still with a separate cooling coil condenser [32]. The investigation and performance analysis of solar still with energy storage materials were massively explored and readers recommended to explore the existed literature for better understanding [33–35].

1.3. Research Significant and Motivation

In low-latitude areas less than $10°$ in latitude angle, the solar radiation that goes into the solar still increases as the cover slope of the approaches the latitude angle [36]. However, the amount of water that is condensed and then falls toward the solar-still basin is also increased in this case. Consequently, the solar yield still is significantly decreased, and the accuracy of the prediction method is affected. Certain studies have attempted to address these problems by reducing the amount of falling water, which has been accomplished by ensuring that the cover slope of the still cover is at least $10°$ [37,38]. However, the magnitude of solar radiation that penetrates the cover of the still and the hourly yield of the still are reduced when the inclination angle is adjusted. This issue was addressed in our previous study [39], which showed that employing rubber scrapers improves productivity by 63% when used in a double-slope solar still in comparison with similar solar still but without using the rubber scrapers for the same climate conditions.

Another challenge in the literature is how to estimate the hourly yield of solar still (HYSS) accurately. A research proposed a mathematical formula that came with a theoretical framework for predicting the stills' heat and mass transfer [40]. The model used simple assumptions but has nevertheless been widely used for a long time as a tool that accurately and conveniently predicts the solar stills' yield under ordinary operating conditions.

However, this framework produces incorrect forecasts for high yields, particularly at high temperatures [41]. Other researchers subsequently established new models by modifying this technique with additional limitations and/or assumptions [42–44]. Meanwhile, several yield forecasting models such as Kumar and Tiwari's and Dunkle's give low accuracy due to the use of traditional procedures that involve substantial amounts of trial and error for determining the necessary constants for the model.

In our previous study [45], the productivity of the DSSSHS was improved, and the mathematical models worked on predicting the productivity of the DSSSHS by adopting a fixed number of rubber scraper movements per hour (4 *NSM*).

In the current study, the change in the *NSM* (1-7 *NSM*) was taken into consideration to identify the ideal *NSM* to obtain the maximum productivity of the DSSSHS, and thus developing a novel and simple model for accurate estimation of the distilled water yielded from the DSSSHS every hour. The new model is more accurate than the previous one, in which the *NSM* enters as a part of the mathematical equation for calculating the productivity of the DSSSHS. This newly developed model is the first to incorporate the impact of *NSM* on the estimation of *HYSS*.

1.4. Research Problem Statement and Objectives

Furthermore, most extant works do not combine accurate optimization methods and experimental yields in constructing hourly yield prediction models for solar stills. They built their models using traditional trial-and-error procedures without considering the amount of water that condenses on the still's cover and falls down the trough of the still, particularly in covers of small slopes, thus estimating HYSS inaccurately. We addressed these problems in our prior study [45], wherein the combined use of rubber scrapers and the particle swarm optimization (PSO) successfully predicted HYSS depending on accurate experimental values of the distilled water. Although our previous study has considered the effect of using rubber scrapers on the productivity of the DSSSHS and the accuracy of the yield prediction model, the time interval between every two scrapes of the condensed water toward the gathering containers, i.e., the effect of the NSM, was not taken into consideration both for the productivity of the solar still and yield prediction model, because leaving water drops that condensed on the inner side of the condensing cover without collection results in more drops falling down into the basin of the solar still. Therefore, the productivity of the solar still will be reduced, which in turn reduces the accuracy of the yield prediction model.

This research further develops the PSO–HYSS model, built in our previous work [45], to consider the impact of the number of scraper motions in an hour (*NSM*). To achieve this goal, this study uses different *NSM* values, namely 1–7, i.e., two other constants *z* and *f* that are concerning to the *NSM* are also used for developing the PSO–HYSS model for accommodating the number of rubber scraper motions. Using these constants is necessary for formulating an accurate formula for estimating the hourly yield of the double-slope solar still hybrid with rubber scrapers (DSSSHS). The main objective of this study is to develop a novel and simple model for accurately estimating the distilled water yielded from the DSSSHS every hour. The new model is more accurate than the previous one, in which the *NSM* enters as a part of the mathematical equation for calculating the productivity of the DSSSHS. This newly developed model is the first to incorporate the impact of *NSM* on the estimation of *HYSS*.

2. Methodology

As a matter of fact, remaining condensed water on the inner surface of the solar still for relatively long period without collecting it in the collection container leads to water loss. This is due to the partial water evaporation owing to the sunlight penetrating from the cover of the still. This also might be due to the falling of condensed water droplets towards the basin of solar still by gravity. Therefore, it is necessary to collect the water condensate after an appropriate period of its formation in which increases the amount of water produced. This will also increase the accuracy of the productivity prediction model

due to the estimated and measured water quantities being very close together. For this purpose, the number of scraping times condensed water will be controlled, leading to increase in productivity. In addition, the number of the movement times of the scrapers will be added to the formula that used the productivity of the solar still for calculating, which increases the accuracy of the yield prediction model.

2.1. Heat and Mass Transfer Mechanisms in Solar Still

Solar radiation and climate parameters are the elements influencing the mechanisms of heat transfer inside the solar still. When solar radiation passes through the atmosphere, a certain amount of the radiation becomes absorbed, reflected, or scattered by the atmosphere, gases, condensed water vapor, and dust.

Heat transfer in the solar still may be external or internal. External heat transfer is controlled primarily by convection, conduction, and radiation, which are independent of each other and are out of the scope of the present study. Evaporation and convection, coupled together with the radiation, cause the internal heat transfer. Salty water which is placed in the solar still's trough is heated through solar energy and then evaporated. Then, the vapor is transferred unobstructed from the salty water surface toward the condensing glass cover by the buoyancy force caused by the decreased density. The difference between the temperature of the condensing cover and that of salty water circulates the water vapor enclosed within the solar still, thereby causing mass and heat transfer resulting from the natural convection.

2.1.1. Convective Heat Transfer from Water to Condensing Glass Cover

The water vapor inside the solar still varies in density, which creates buoyancy force. This force ultimately causes the interior of still to undergo convective heat transfer. The expression of this phenomenon takes place from the water surface toward the condensing cover [Q_{cw} (W/m^2)] is provided by the following general equation [46]:

$$Q_{cw} = h_{cw} \times A_w \times (T_w - T_g) = h_{cw} \times A_w \times \Delta T, \tag{1}$$

where h_{cw} represents the convective heat transfer coefficient that takes place from the salty water toward the condensing cover of the still $\left(\frac{W}{m^2 \cdot {}^\circ C}\right)$, A_w represents the salty water's surface area (m^2), and ΔT is the difference in temperatures of the glass cover of the still and the salty water included in the trough of the still (°C). h_{cw} represents a function of fluid properties, operating temperatures, still geometries, and flow characteristics. The relationship between the convective heat transfer coefficient and the expression of the Nusselt number (Nu) can be illustrated as [47]

$$Nu = (h_{cw} \times d)/K = C \times (Gr \times Pr)^n, \tag{2}$$

where d is the characteristic length of solar still (m); this variable can be considered the average distance between the brine interface and the condensing glass cover. Thus, the glazing configuration and the solar still geometry determine this length [41]. *Pr* and *Gr* are the Prandtl and Grashof numbers, respectively (dimensionless), and *n* and *C* are constant parameters (dimensionless). These constants can be calculated using linear regression analysis [47]. The thermal conductivity of the water vapor inside the solar still is denoted by *K* (W/m·K). The following equation expresses the coefficient of convective heat transfer from the salty water to the still condensing glass cover [48]:

$$h_{cw} = \frac{C \times K}{d}(Gr \times Pr)^n. \tag{3}$$

The Grashof and Prandtl numbers can be expressed by [48]:

$$Gr = \frac{(g \times \beta \times d^3 \times \rho_v^2 \times \Delta T)}{\mu^2}, \tag{4}$$

where g represents gravitational acceleration which is equal to 9.807 m/s^2, β indicates the coefficient of the volumetric thermal expansion (K^{-1}), ρ_v denotes the mass density of the water vapor inside the solar still (kg/m^3), ΔT is the difference between the temperatures of the surface of the water and the cover (°C), and μ depicts the viscosity of the water vapor inside the solar still (N·s/m^2) [48].

$$Pr = \frac{\mu \times C_v}{K}, \tag{5}$$

where C_v represents the specific heat of water vapor inside the solar still (J/kg.°C). The physical properties of water vapor inside the solar still, which are temperature-dependent, were determined by [48], and can be expressed as follows:

$$K = 0.0244 + 0.7673 \times 10^{-4} \times T_v, \tag{6}$$

$$\rho_v = 353.44/(T_v + 273.15), \tag{7}$$

$$\beta = 1/(273.15 + T_v), \tag{8}$$

$$\mu = 1.718 \times 10^{-5} + 4.620 \times 10^{-8} \times T_v, \tag{9}$$

$$C_v = 0.1434 \times T_v + 1.101 \times 10^{-4} \times T_v^2 - 6.7581 \times 10^{-8} \times T_v^3 + 999.2, \tag{10}$$

$$h_{fg} = \left[1 - \left(7.616 \times 10^{-4} \times T_v\right)\right] \times 3.1615 \times 10^6, \text{for } T_v > 70\,°\text{C}, \tag{11a}$$

$$h_{fg} = 2.4935 \times 10^6 \times \left(1 + 1.3132 \times 10^{-7} \times T_v^2 - 4.7974 \times 10^{-9} \times T_v^3 - 9.4779 \times 10^{-4} \times T_v\right), \text{for } T_v < 70\,°\text{C}. \tag{11b}$$

Dunkle's model expresses the coefficient of the convective heat transfer $\left[h_{cwD}\left(\frac{\text{W}}{\text{m}^2.°\text{C}}\right)\right]$ from salty water toward the condensing cover of still as [40]

$$h_{cwD} = 0.884 \times \left[(T_w - T_g) + \frac{(P_w - P_g)}{268.9 \times 10^3 - P_w} \times (T_w + 273.15)\right]^{\frac{1}{3}}. \tag{12}$$

DSSSHS is running in the passive mode in this study. Thus, the convective heat transfer coefficient from the salty water toward the condensing cover under Clark's model $\left[hcwCL\left(\frac{\text{W}}{\text{m}^2.°\text{C}}\right)\right]$ is the same as that for Dunkle's model, which is determined by using Equation (12) [49], while that from the salty water toward the condensing cover under the model of Kumar and Tiwari $\left[hcwKT\left(\frac{\text{W}}{\text{m}^2.°\text{C}}\right)\right]$ can be determined by using values of n and C, which are equal to 0.4114 and 0.0322, respectively, in Equation (3) [47].

2.1.2. Evaporative Heat Transfer from Salty Water toward the Condensing Cover

The amount of distilled water is calculated by [50]

$$m_{ew} = \frac{q_{ew} \times A_w \times t_{int}}{h_{fg}}, \tag{13}$$

where

$$q_{ew} = h_{ew} \times (T_w - T_g), \tag{14}$$

and

$$h_{ew} = 16.23 \times 10^{-3} \times h_{cw} \times \frac{P_w - P_g}{T_w - T_g}, \tag{15a}$$

where A_w represents the surface area of salty water (m^2), t_{int} is the time-interval (s), and h_{fg} indicates the latent heat of water vaporization (J/kg). Dunkle's model which expresses the coefficient of the evaporative heat transfer $[hewD\left(\frac{\text{W}}{\text{m}^2 \cdot °\text{C}}\right)]$ which occurs from the salty water toward the condensing cover can be expressed as [48]

$$h_{ewD} = 16.23 \times 10^{-3} \times h_{cwD} \times \frac{P_w - P_g}{T_w - T_g}. \tag{15b}$$

P_g and P_w are expressed by [48,51], as follows:

$$P_w = e^{(25.317 - 5144/(T_w + 273.15))}, \tag{16}$$

$$P_g = e^{(25.317 - 5144/(T_g + 273.15))}. \tag{17}$$

By inclusion of Equation (3) into Equation (15a) we can rewrite h_{ew} as:

$$h_{ew} = 0.01623 \times \frac{K}{d} \times C \times (Gr \times Pr)^n \times \left[\frac{(P_w - P_g)}{(T_w - T_g)} \right]. \tag{18}$$

Meanwhile, incorporating Equations (14) and (18) into Equation (13) rewrites m_{ew} as follows:

$$m_{ew} = \frac{0.01623}{h_{fg}} \times \frac{K}{d} \times A_w \times t_{int} \times C \times (P_w - P_g) \times (Gr \times Pr)^n. \tag{19}$$

The coefficient of evaporative heat transfer from the salty water toward the condensing cover of the still and the distilled water amount in the models of Kumar and Tiwari and Dunkle's are estimated by incorporating their n & C values, which are 0.4114 & 0.0322 and 0.334 & 0.075, into Equations (18) and (19), respectively [47]. Meanwhile, the rate of the evaporative heat transfer from the salty water toward the condensing cover in Clark's method $\left[qewCL\left(\frac{\text{W}}{\text{m}^2 \cdot °\text{C}}\right) \right]$ is expressed as [49]

$$q_{ewCL} = K/2h_{cwCL}(P_w - P_g), \tag{20}$$

where $K = 0.016273$. By incorporating Equation (20) into Equation (14), the coefficient of evaporative heat transfer from the salty water toward the condensing cover under Clark's model $\left[hewCL\left(\frac{\text{W}}{\text{m}^2 \cdot °\text{C}}\right) \right]$ is expressed as [49]

$$h_{ewCL} = K/2h_{cwCL}(P_w - P_g)/(T_w - T_g). \tag{21}$$

2.2. Developed PSO–HYSS Model

Different researches were conducted to enhance the yield and thermal performance of the solar stills. Several models have also been developed and conducted to estimate their yield. However, most of these models suffer from several limitations that reduce their estimation accuracy versus the actual measurements.

The current research develops a novel and simple model for estimating the distilled water yielded from the DSSSHS every hour in areas at low latitudes. This newly designed model is the first to incorporate the impact of *NSM* on the estimation of HYSS. Equation (19) can be modified as follows:

$$m_{ew} = (z + f * \log(NSM)) * \frac{16.23 \times 10^{-3}}{h_{fg}} \times \frac{K}{d} \times A_w \times t_{int} \times C \times (P_w - P_g) \times (Gr \times Pr)^n. \tag{22}$$

The proposed model is created by determining the values of f and z unknown constants related to NSM and those of n and C related to the Nusselt number expression (*Nu*). These constants are to be used in formulating the models for estimating HYSS. The resolution of

the optimization problem can determine these constants through PSO; the optimum values of; *f*, *z*, *n*, and *C* unknown constants are estimated to determine the optimal yields.

This technique, which includes the effect of *NSM* in building the yield prediction model, further improves estimation accuracy. The proposed model is verified against the data gathered by the experiments in this study and then compared with several existing models. The predicted yield is compared with the yields experimentally obtained from the current research and from the models of PSO–HYSS, regression, Dunkle's, Clark's, and Kumar and Tiwari's models for the verification of the thoroughness of the new improved model.

2.3. Hourly Yield Model for the DSSSHS Created Employing PSO

PSO is a computational method that is easier to implement and has fewer parameters than genetic algorithms. This is better than other evolutionary algorithms in solving several optimization problems [52]. Therefore, in the current model, unknown *f*, *z*, *n*, and *C* constants that are used to establish the formula that estimates HYSS are calculated using the PSO algorithm. This algorithm is used in the present study to evaluate the optimum values of constants *f*, *z*, *n*, and *C*, the set of unknown coefficients expressed in Equation (22). The HYSS model is optimized using the PSO algorithm. Three parameters are considered before model optimization, namely formulating all objective functions, optimizing the model through PSO, and using the criteria for convergence. The subsequent sections discuss these parameters.

2.3.1. Objective Functions

The current study optimizes the developed PSO–HYSS model. It determines the optimum values of *f*, *z*, *n*, and *C* that constitute the set of the unknown coefficients in the model using PSO algorithm. Moreover, after identifying the coefficient set that can make the objective function as minimum as possible, the search process is terminated to determine the convergence of the present model. The simulation and optimization of the developed PSO–HYSS model for DSSSHS is conducted using MATLAB. Applied objective functions are the mean absolute percentage error (*MAPE*), the root mean square error (*RMSE*), and the mean absolute error (*MAE*). These are calculated as follows [53,54].

i. Mean absolute error (*MAE*)

The metric presents the computed average error between the predicted and observed values. The mathematical expression is given in Equation (23) [55]:

$$MAE = \frac{1}{NS} \sum_{j=1}^{NS} |y - \acute{y}|, \tag{23}$$

where $\acute{y}$ and y are the predicted and actual values, respectively, and *NS* represents the number of data samples used in the current study.

ii. Mean absolute percentage error (*MAPE*)

This statistical measure is used to evaluate the effectiveness of the prediction models since it imparts relative values. The *MAPE* efficiently identifies the relative differences between models because it is unaffected by the size or unit of the actual and predicted values. *MAPE* can be calculated using Equation (24) [56]:

$$MAPE = \frac{1}{NS} \sum_{j=1}^{NS} \left| \frac{y - \acute{y}}{y} \right|. \tag{24}$$

iii. Root mean square error (*RMSE*)

RMSE is determined to compute the square error of the forecasting in comparison with the actual values and determine the square root of the summation value. Thus, *RMSE* is the average distance of a data point from a fitted line measured along a vertical line.

This tool efficiently identifies undesirably significant differences. *RMSE* is determined as follows [57]:

$$RMSE = \sqrt{\frac{1}{NS} \sum_{j=1}^{NS}(y - \acute{y})^2}. \tag{25}$$

2.3.2. Particle Swarm Optimization (PSO) Algorithm

The primary PSO algorithm is an evolutional calculating method proposed by [58] and inspired by the birds' flocking behavior (particles). PSO is often utilized because it is robust and exhibits global convergence capability and easy application [59,60].

The PSO algorithm was used effectively to solve several optimization problems [61–63]. Shi and Eberhart [64] proposed that the convergence rate of PSO be improved with the use of inertial weight (w). This technique helps update the previous velocity value of the particle contribution rate to their current one. The position, in addition to the velocity of each particle, can be updated throughout the search based on Equations (26)–(27) as follows [65]:

$$V_i(t+1) = w \times V_i(t) + c_1 \times Rand(\cdot)_1 \times [pbest_i(t) - X_i(t)] + c_2 \times Rand(\cdot)_2 \times [gbest_i(t) - X_i(t)], \tag{26}$$

$$X_i(t+1) = X_i(t) + V_i(t+1), \tag{27}$$

where V_i and X_i represent the velocity and location, respectively, of the particles under investigation; in general, $Rand(\cdot)_1$ and $Rand(\cdot)_2$, which denote random numbers which are regularly distributed between 0 and 1, are considered equal; c_1 and c_2 are the coefficients of acceleration, and *pbest* and *gbest* are the best location and global position, respectively, for each studied particle. c_1 and c_2 refer to the "trust" settings, which denote the confidence's degree in the best solution obtained by individual particles (c_1; cognitive parameter) or the whole particle swarm (c_2; social parameter). The exploratory capability of the swarm is partly controlled by inertial weight, which is a scaling factor that appeared as w in Equation (26). Moreover, w scales the value of the current velocity, affecting the velocity vector in its revised value. The first PSO algorithm was used by [58] not containing the inertial weight, which was only subsequently used by [64] to modify the PSO convergence rate. Particle velocity consists of three vectors which are the inertial, cognitive, and social components. The inertial (momentum) component is the first vector and depends on the particle's velocity at a former time stage while allowing the particle to keep along its present path. The second vector illustrates the cognitive (memory) component, which is derived according to the best location of the particle through all iterations while also allowing the particles to gravitate to their best previous positions. Finally, the third vector is the social (swarm) component, which assists the particles in gravitating to the best locations in the swarm.

2.3.3. Convergence Criteria

The search process in PSO is a repetitive procedure; the optimization process has to be stopped by applying a convergence criterion. This study selects two convergence criteria: minimum error permitted and the maximum iterations' number of PSO during the estimation of optimum values of the objective functions. The maximum number of iterations depends on how complex a problem is, whereas the minimum error permitted is based on an assumption of prior knowledge of the global optimized value. Table 1 lists several major parameters for PSO, whereas the different convergence parameters are explained in Table 2 used for the PSO algorithm in the current study.

Table 1. Major parameters for PSO algorithm.

Parameter	Description
Dimension of particles, D	This parameter is calculated by the problem to be optimized.
Social and cognitive parameters	$c_1 = 1.494 = c_2$ [66]. Other values can also be used, on condition $0 < (c_1 + c_2) < 4$.
Particles' number, N	The range is from 10 to 40 but can be increased to 50–100 for certain complex or special problems.
Vectors including the upper and lower bounds of the D design variables, which are x^L and x^U, respectively	The optimization problem calculates these vectors. Various ranges can generally be applied for different particle dimensions.
Inertial weight, w	w is usually < 1; however, $w = 0.7$ is considered to improve convergence speed [66].

Table 2. Convergence parameters for PSO algorithm.

Parameter	Description
Maximum number of iterations (T) for the termination criterion	This number is specified by the complexity of the optimization problem and other algorithm parameters of PSO (N, D).
The number of iterations kf for which the relative improvement of the objective function meets the convergence check Iterations.	Convergence is considered achieved when the relative improvement of the objective function over the last kf iterations (including the current iteration) is less than or equal to fm.
Minimum relative amelioration (fm) of the value of the objective function	

2.4. Implementing PSO with HYSS Model

The assumption that is made for estimating *f, z, n,* and *C* constants is critical to obtaining an accurate prediction model. By implementing PSO, the optimized solution can be found by determining the optimal values of *f, z, C* and *n*. Consequently, the improvement of the model performance is achieved. This study integrates the HYSS with the PSO algorithm for creating a hybrid model called the developed PSO–HYSS.

This technique is expected to reduce the difference between forecasted and actual values of the HYSS to minimum values. PSO is applied in the present work by using MATLAB software. Each swarm includes the unknown constants *f, z, n,* and *C*. The best values obtained for *f, z, n,* and *C* are utilized in the developed PSO–HYSS model to reduce the error in predicting the hourly yield. Appendix A illustrates the flow diagram for the developed PSO–HYSS model that represents the main structure of the hybrid model used to increase the prediction accuracy of the hourly yield.

PSO is implemented to estimate the optimal hourly yield as follows:

i. After a random position is specified for each particle in the space, the swarm is initialized.
ii. In the developed PSO–HYSS model, the objective function of each particle is evaluated.
iii. For each particle, the objective function's value is then matched with the value of its *pbest*. The current value is set as *pbest* if the former is better than the current *pbest* value. Meanwhile, $pbest_i$ represents the current position of the particle X_i.
iv. The particle whose objective function has the best value is named as *gbest*, and its position is presented by $gbest_i$.
v. Equations (26) and (27) are used to modify particles' positions and velocities.
vi. The steps from 2 to 5 are repeated till reaching the maximum number of iterations or achieving a satisfying value of the objective function.

A total of two hundred sixty-two datasets are gathered for twenty-four days for different water depths, *NSM*, and climatic conditions, with a fixed east-west orientation. These datasets are applied for building and verifying the modified PSO–HYSS model for the DSSSHS. All data which are obtained during the experiments include these of the one hundred thirty datasets gathered during 12 days (30 March 2016; 31 March 2016; and 1–15 April 2016) from our previous experiments [39,45], and the one hundred thirty-two datasets collected for another 12 days (3, 4, 9–11, 16–19, 20, 25 and 26 February 2017) from the current experiments.

Data are segregated into verification and construction groups. In the construction group, the proposed model is constructed using the two hundred seven datasets which are collected during nineteen days (30 and 31 March 2016; 3, 4, 8, 9, 11 and 13–15 April 2016; and 4, 9–11, 17–20 and 25 February 2017). The proposed model is verified in the verification group using the fifty-five datasets collected for five days (1 and 2 April 2016, and 3, 16, and 26 February 2017). A theoretical model is built to forecast the HYSS of the DSSSHS under the previously mentioned conditions. The modified model is created by determining the best values for *n* and *C* for the *Nu* expression and *z* and *f*, which are associated with the *NSM*. Those constants have been used for formulating the relation for forecasting the HYSS.

Experimental values are compared with the forecasted ones from the mathematical models. This comparison is used to find how accurate those models are. Experimental values for the HYSS are also compared with those forecasted using Kumar and Tiwari's, Clark's, and Dunkle's, models. These are calculated from our previously established PSO–HYSS and regression models [30,36]. The comparison was conducted to show that the accuracy of the newly developed PSO–HYSS model in forecasting the HYSS of DSSSHS is better than that of related models in the literature.

The effectiveness and consistency of the developed PSO–HYSS model are tested through statistical analysis. The performance of the proposed model is computed using a performance index (*PI*) that was focused on by [67]. This index considers the model performance as a function of the relative *RMSE* (*RRMSE*) and the correlation coefficient (*R*). *PI* and *RRMSE* are computed as follows [68]:

$$PI = RRMSE/(R + 1), \tag{28}$$

where

$$RRMSE = \frac{1}{|y_{av}|}\sqrt{\frac{1}{NS}\sum_{j=1}^{NS}(y - \acute{y})^2}, \tag{29}$$

where y_{av} represents the average actual value, and

$$R = \frac{\sum_{i=1}^{NS}(y - y_{av})(\acute{y} - \acute{y}_{av})}{\sqrt{\sum_{j=1}^{NS}(y - y_{av})^2\sum_{j=1}^{NS}(\acute{y} - \acute{y}_{av})^2}}, \tag{30}$$

where $\acute{y}_{av}$ represents the average predicted value. The range of *PI* value is between 0 and +∞. Better model performance is achieved for a smaller value of *PI*. A *PI* value that is nearest to 0 refers to that model forecasting approximate actual values and is therefore regarded to be within the acceptance threshold [67].

A criterion set is acquired from [69] for external validation and data testing of the proposed model. The criteria can be presented as follows: first, *k* or *k'* which represents the gradient of the regression line between actual data (*y*) and predicted data (*ý*) is close to 1; second, the performance indexes $|np|$ and $|mp|$ are both less than 0.1. An index (R_m) was expressed by [70] to evaluate the external predictability of models. The corresponding validation criterion of R_m should be less than 0.5. The validation conditions for the models are shown in Table 3.

Table 3. Statistical models proposed and the necessary validation conditions.

Item	Formulas	Conditions
1	R, Equation (30)	$R > 0.8$
2	$k = \dfrac{\sum_{j=1}^{NS}(y \times ý)}{y^2}$	$0.85 < k < 1.15$
3	$k' = \dfrac{\sum_{j=1}^{NS}(y \times ý)}{ý^2}$	$0.85 < k' < 1.15$
4	$R_m = R^2 \times \left(1 - \sqrt{\left|R^2 - Ro^2\right|}\right)$	$R_m > 0.5$
5	$mp = \dfrac{\left(R^2 - Ro^2\right)}{R^2}$	$\|mp\| < 0.1$
6	$np = \dfrac{\left(R^2 - Ro'^2\right)}{R^2}$	$\|np\| < 0.1$

As shown in Table 3, Ro^2 and Ro'^2 can be estimated as [71]

$$Ro^2 = 1 - \frac{\sum_{j=1}^{NS}(ý - yo)^2}{\sum_{j=1}^{NS}(ý - ý_{av})^2}, \; yo = k \times ý, \tag{31}$$

$$Ro'^2 = 1 - \frac{\sum_{j=1}^{NS}(y - ýo)^2}{\sum_{j=1}^{NS}(y - y_{av})^2}, \; ýo = k' \times y, \tag{32}$$

where Ro'^2 and Ro^2 represent the R^2 that passes over the origin between the experimental and predicted values and between the predicted and observed values, respectively. Furthermore, R and $RRMSE$ represent the parameters to evaluate the yield predicting models.

3. Experimental Database

3.1. Setup of the Experiment

In the current study, a DSSSHS is developed, tested, and operated to improve HYSS and construct the modified PSO–HYSS. This proposed model's ultimate goal is to predict HYSS accurately. Similar to those in our previous studies [39,45], the DSSSHS system in the present study comprises rubber scrapers, but with *NSMs* of 1–7. Scraper motions are operated with the aid of two 12 V DC motors supplied with 150 Ah batteries which are recharged by a photovoltaic panel (12 V, 200 W/h DC). In addition, the system includes a feed tank with salty water. Non-transparent aluminum sheets comprise the tank surfaces. Ambient air is counteracted by insulating the external tank surfaces, except for the one facing the sun, with 0.019 m thick nitrite foam insulation sheets. Their density and thermal conductivity are 70 kg/m^3 and 0.038 W/m·K, respectively. The tank surface fronting the sun is colored with black to improve the absorption of solar radiation. The improved absorption increases the water temperature inside the feeding tank for the heat transfer by conduction between the tank and water.

A water hose made from PVC was used in the system. This hose is insulated using a 0.01 m thick insulation pipe made from nitrite foam to counteract ambient air. The specifications of the insulation pipe are the same as those of the insulation sheets mentioned before. The hose is affixed to the feeding tank and is used to feed the solar still with salty water using a floating valve. Two colored rulers are affixed onto opposite surfaces of the DSSSHS to aid in-depth adjustments of the salted water.

Thermocouples (K-type, Omega Engineering, Manchester, UK) are still attached to the solar using adhesive tape. These thermocouples are linked to a data logger (GL 800, Graphtec Corporation, Yokohama, Japan) for recording the temperatures each 5 min during the daytime. The thermocouples are used for the measurement of the temperatures of the salty water (T_w), water vapor within the solar still (T_v), and glass cover on the two sides of the cover (T_{g1} and T_{g2}). The overall glass cover temperature (T_g) is the mean value of T_{g1} and T_{g2}. Small pieces of aluminum foil were used to cover these two thermocouples

to reflect the direct sun radiation and obtain proper readings of T_{g1} and T_{g2}. Appendix B shows an isometric diagram of DSSSHS in which the arrangement of the thermocouples is illustrated.

An electronic balance (EK6100i, A&D Co., Ltd., Tokyo, Japan) is used for measuring the amount of the HYSS. A pyranometer (Model 8–48, Eppley Laboratory Inc., Newport, USA) is used for measuring solar radiation. Table 4 lists the instruments that are used for the onsite experiments. The dimensions of the base of the solar still are $1000 \times 1000 \times 30$ mm (LWH). The dimensions of the glass sides are 1000×100 mm (LH) for two opposite sides and 1000×100–126.2 mm (length, variable height) for the two opposite sides. The area of the basin of the solar still is 1 m^2. The internal surfaces of the solar still trough is colored with black paint to increase their absorptivity. The density, thermal conductivity, and thickness of the trough are 2710 kg/m^3, 222 W/m.K, and 3 mm, respectively. The solar still basin's base and sides are insulated using the same insulation sheets described before.

Table 4. Main measurement instruments that are used in the experiments.

Instrument	Model	Accuracy	Range
Medi-logger			
	GL800 Graphtec Corp.	Temperature—K type ±0.05% of the reading Voltage ±0.1% of reading	Temperature—K type −200 °C to +1370 °C Voltage −22 mV to +22 mV
Pyranometer			
	8–48 Eppley Laboratory, INC.	±30 W.m^{-2}	0 W.m^{-2} to 2195 W.m^{-2}
Compact digital scale			
	EK-6100i A and D Company, Ltd.	±0.2 g	0 to 6000 g
Thermocouple			
	K type Omega Engineering	±0.1 °C	−200 °C to +1250 °C

Four inclined PVC channels for collecting water are used to direct the distilled water toward two PVC containers, each of 3 L capacity. A 0.2 and 0.5 mm thick clear glass forms the condensing cover of solar still. The condensing glass cover's density and thermal conductivity are 2500 kg/m^3 and 0.96 W/m.K, respectively. The cover is affixed to the sides of still at an angle equal to 3° with the horizontal; this slope was chosen to increase the amount of the solar radiation penetrating the solar still to its maximum value. Two rubber scrapers were used for scraping water condensate on the internal sides of glass cover

towards the collection channels and then into PVC containers. The DSSSHS is mounted on a hollow iron column of circular section with dimensions of 1100×100 mm (LD). This column can be fully rotated horizontally by $360°$. Two electrical boards control the time intervals, speed, and direction of rubber scrapers. The current study uses different NSMs (1–7) at a speed equal to 0.2 m/s.

The electrical boards comprise delay relay timers, resistances, a basic micro-switch, general relays, and a wiring system. Electrical boards are run using two batteries $(DC - 12\ V - 150\ Ah)$. An aluminum water guide is attached under each scraper to reduce the amount of condensed water that can be lost during the motion of scrapers. The slope orientation of the aluminum guides effectively directs the collected water toward the inclined collecting channels.

3.2. Experimental Results

PSO–HYSS model from our previous study [45] is modified to consider the effect of *NSM*. Additional constants (f and z) are applied in the modified PSO–HYSS model to include the effect of NSM. Constants related to NSM are used in the estimating equation of the HYSS (Equation (22)).

A total of two hundred sixty-two datasets are gathered during the daytime (09:00–19:00) for 24 days (30–31 March 2016; 1–4, 8–9, 11 and 13–15 April 2016; and 3–4, 9–11, 16–20 and 25–26 February 2017). Based on these datasets, the modified PSO–HYSS model for DSSSHS is constructed and verified. The datasets are classified into two groups. The first one includes 207 datasets (total of 19 days: 30–31 March 2016; 3–4, 8–9, 11 and 13–15 April 2016; and 4, 9–11, 17–20 and 25 February 2017) and is utilized to build the suggested model. The second group, which includes 55 datasets (total 5 days: 1–2 April 2016, and 3, 16 and 26 February 2017), is used to verify the model.

The following are the parameters that are used for calculating the theoretical internal heat transfer coefficients for evaporation and convection: experimental yield, characteristic length of solar still, *NSM*, and the temperatures of the water vapor within the still, salty water, and the glass cover. In all experiments, the still is directed in the east-west orientation. Experiments are conducted between 09:00 and 19:00 for 24 days. Salty water temperature, the temperature of the water vapor within the solar still, and glass cover temperature are measured with thermocouples and then logged every 5 min. The averages of the hourly yields are recorded and calculated. Experiments are conducted on three salty water depths (30, 19, and 10 mm) and 7 cycle motion counts from 1 to 7 for the rubber scrapers. The temperatures mentioned above, water depths, experimental HYSS, and the solar still's characteristic length are recorded. The experimental data in Appendix C (19 days) are used to construct the model, and those in Appendix D (remaining 5 days) are used to verify the model.

Appendix C shows the condensing cover temperature, the water vapor temperature within the solar still, and the salty water temperature peak at 58.20, 72.00, and 77.80 degrees Celsius, respectively. Glass and ambient temperatures continuously increase from early morning until they reach their maximum values at midday. The temperature rise extends from 13:00 to 16:00 and decreases toward the sunset. A considerable difference between the temperatures of the salty water and those of the condensing cover of the still is also noticed in the daytime (Appendix C). The difference between these temperatures is directly proportional to the amount of the HYSS.

Results show that the highest temperature difference occurred from 13:00 to 17:00, which suggests that more water is produced within this timeframe than at other periods. This finding further implies that water production is enhanced by rising the variations in temperature between the evaporative and condensing surfaces. In several instances, the maximum HYSS is observed between 15:00 and 17:00; yields generally depend on the daily distribution of solar radiation and the depth of salty water. As shown in Appendix D, glass and water vapor temperatures within the still and salty water temperatures reach their maximum values of 58.30, 70.00, and 76.30 degrees Celsius, respectively. Maximum yield

is observed within the period that lasted from 15:00 to 17:00. We can notice clearly that this behavior is similar to the temperature difference explained for the values shown in Appendix C. Table 5 illustrates the mean, maximum, and minimum values of parameters used in building the suggested model.

Table 5. Parameter ranges of the two hundred seven datasets used for developed PSO–HYSS model construction.

Parameters	Mean	Maximum	Minimum
T_g (°C)	43.20	58.20	24.90
T_v (°C)	52.60	72.00	25.30
T_w (°C)	55.60	77.80	26.70
d (m)	0.103	0.108	0.098

Note: T_g is the glass cover temperature, T_v is the temperature of water vapor inside the solar stills, T_w is the saline water temperature, and d is the solar still's characteristic length.

4. Results and Discussion

4.1. Analysis of Developed PSO–HYSS Model

Evaluation of the developed model is fulfilled using different statistical analyses, two of them being the coefficient of variation (*CoV*) and the coefficient of determination (R^2). Furthermore, the three objective functions of *RMSE*, *MAPE*, and *MAE* are considered, and 6 swarm sizes (10 to 60, step 10) are analyzed. Data accuracy is essential in this study because any inaccuracy can affect model performance. Some researchers stated a value of 3 as the minimum ratio between the number of objects and the number of variables that should be chosen for verifying the acceptance of the model, and a value of 5 gives better results than 3 [72]. In this study, this ratio for the developed PSO–HYSS model is 207/4 or 51.75, which is higher than 5, i.e., more than the minimum value.

Formulas $c_1 = c_2 = 1.494$ and $w = 0.7$ can be used to converge the algorithm efficiently. In this scenario, the process of the PSO algorithm is continuously updated until g_{best} is obtained or until a pre-defined maximum number of iterations is reached. Iteration number in the developed PSO–HYSS model is fixed to 2000 because the variance becomes constant after the 1470–1531 iteration range for the three objective functions, namely *RMSE*, *MAPE*, and *MAE*. Then, the PSO parameter settings are employed to verify the PSO algorithm and obtain the specific objective functions of the swarms with 10, 20, 30, 40, 50, and 60 particles. The full procedure is shown in Appendix E.

The different sizes of the swarm are examined to select the best size for the swarm, thereby reducing error and lapse time. As shown in Appendix E, the optimal solution of the PSO algorithm can be obtained with a 30-particle swarm size, for which the minimum values of *RMSE*, *MAPE*, and *MAE* are 0.00062, 0.03898, and 0.01096, respectively. Compared with the 30-particle swarm size, the 10- and 20-particle swarm sizes show higher error rates, whereas the 40-, 50-, and 60-particle swarm sizes involve longer lapse times. The developed PSO–HYSS model obtains the best value of R^2 which is equal to 0.9965 (Figure 1), suggesting that the target values are highly accurate [73].

The relationship between the predicted yield (T_{pre}) and the measured yield (T_{exp}) is examined [74], and a scatter plot is used to visualize the agreement between both yields easily. The differences between the measured values from the forecasted values ($Mexp - Mpre$) of the HYSS are drawn versus their average values $[(Mexp - Mpre)/2]$. The scatter plot presents systematic and random differences which subsequently correspond with the variations in the results.

The plot of the developed PSO–HYSS model (Figure 2) represents a mean value +1.96 and −1.96 of the standard deviation (*SD*); that is, those values can reveal whether the calculations are smaller or larger than the base values. In other words, the relationship between predicted and estimated errors can be calculated because the levels of systematic and random differences are represented as scatter points [74]. Consequently, a good agreement among testing methods is depicted in Figure 2; that is, 96.62 percent of the data

is distributed within the agreement's limits of MAPE (Figure 2b), 96.14 percent for *MAE* (Figure 2a), and 94.2 percent for RMSE (Figure 2c).

(**a**) MAE

(**b**) MAPE

(**c**) RMSE
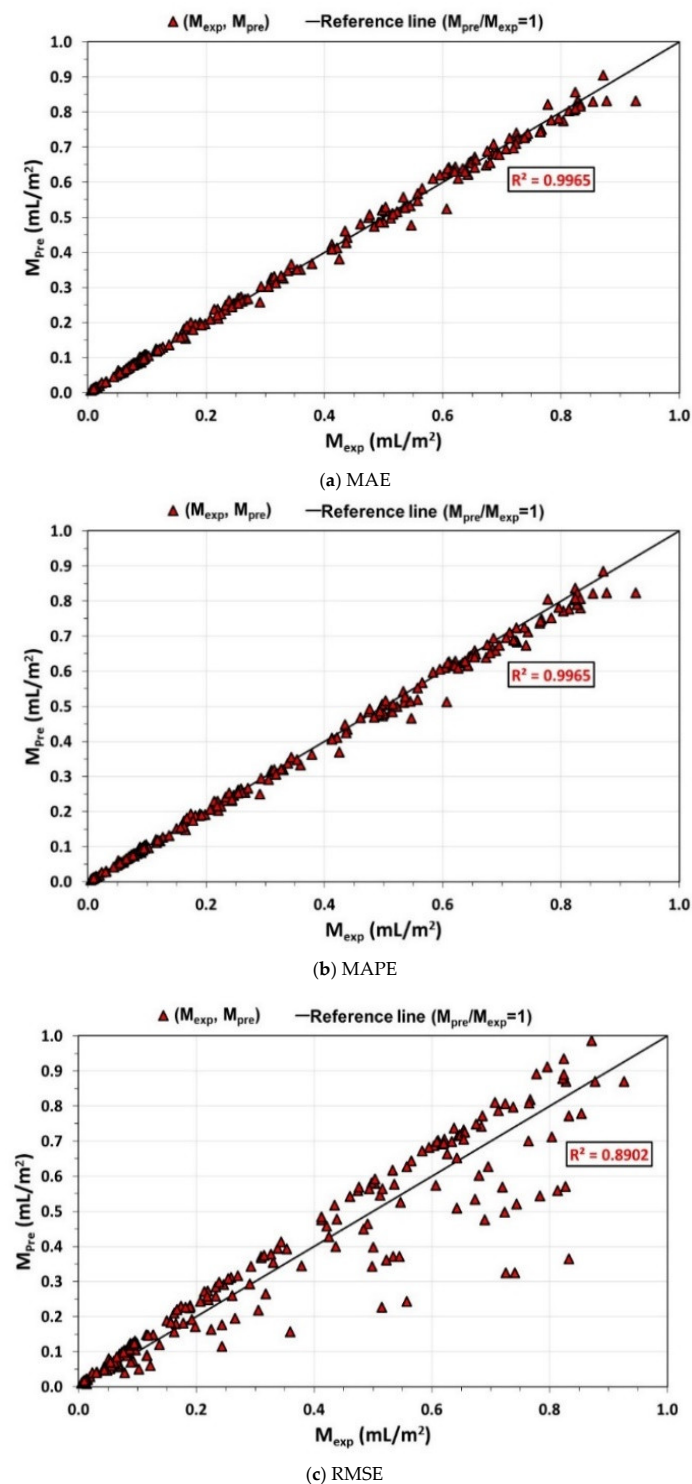
Figure 1. Predicted versus measured HYSS on the basis of developed PSO–HYSS model.

Then, the *CoV and R^2* values are calculated. The *MAPE* objective function shows higher accuracy in terms of estimated HYSS than the RMSE and MAE objective functions. The optimum values of *n*, *C*, *f*, and *z* coefficients of the developed PSO algorithm (Equation (22)) are 0.2172, 0.4705, 0.4978, and 0.0134, respectively. Those coefficients are integrated into the developed PSO–HYSS model.

(**a**) MAE

(**b**) MAPE

(**c**) RMSE
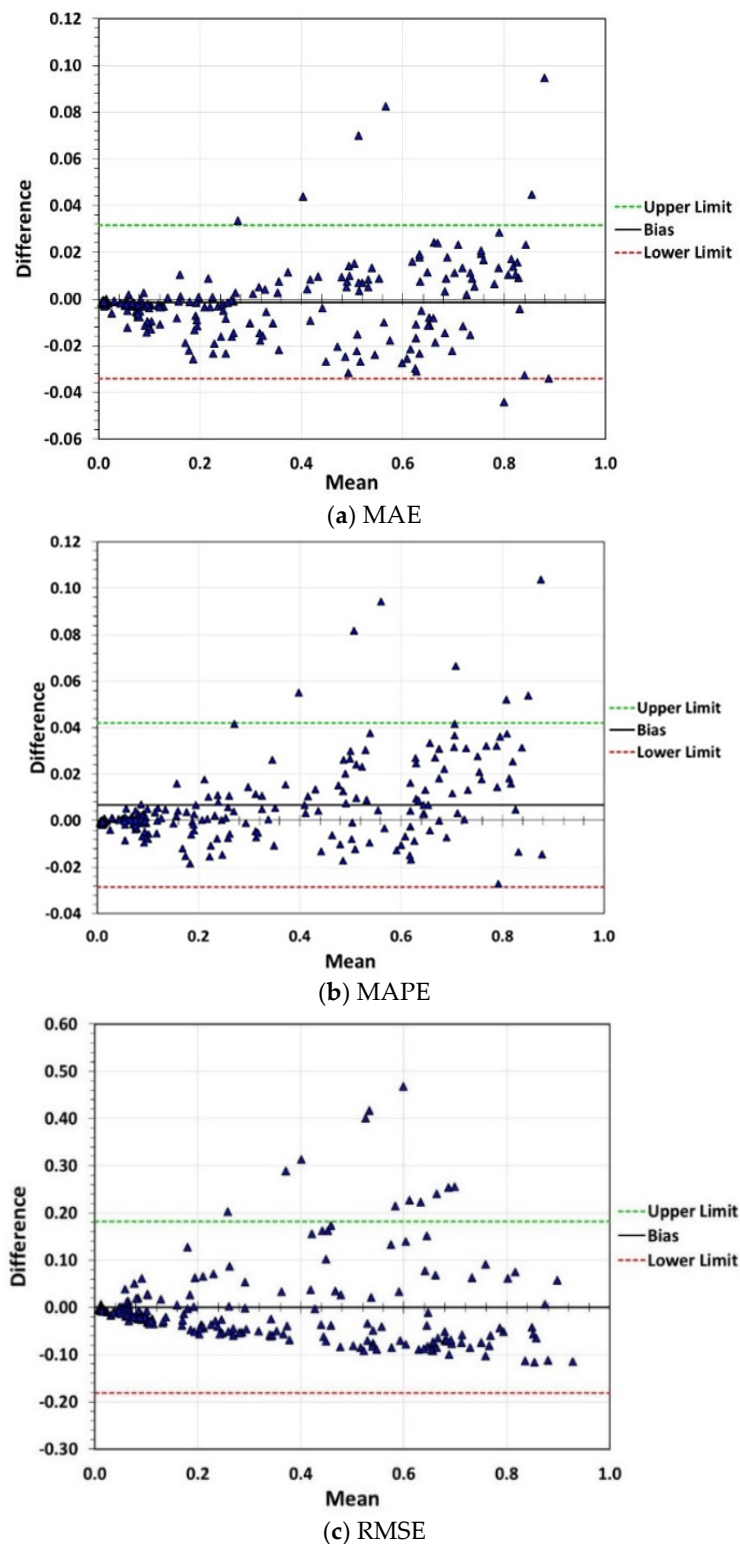
Figure 2. Bland–Altman plot of predicted and measured HYSS using developed PSO–HYSS model.

4.2. Verification of Developed PSO–HYSS Model

The remaining fifty-five experimental datasets are used for verifying the developed PSO–HYSS model (recorded data not used in constructing and optimizing the model). Table 6 lists the values of the HYSS that the developed PSO forecasts the developed PSO–HYSS model forecasts; those values also agreed with experimentally measured values.

Table 6. Comparison between the predicted and measured HYSS values of regression, Clark's, Kumar and Tiwari's, Dunkle's, PSO–HYSS, and the developed PSO–HYSS models.

Date	Time	M_{exp} (L/m²·h)	$M_{Developed\ PSO\ (This\ Study)}$ (L/m²·h)	M_{PSO} (L/m²·h)	M_{Dunkle} (L/m²·h)	$M_{Regression}$ (L/m²·h)	$M_{Kumar\ \&\ Tiwari}$ (L/m²·h)	M_{Clark} (L/m²·h)	$M_{Developed\ PSO\ (This\ Study)}/M_{exp}$	M_{PSO}/M_{exp}	M_{Dunkle}/M_{exp}	$M_{Regression}/M_{exp}$	$M_{Kumar\ \&\ Tiwari}/M_{exp}$	M_{Clark}/M_{exp}
	9:00	0.010	0.009	0.009	0.011	0.010	0.012	0.006	0.91	0.88	1.14	0.98	1.25	0.61
	10:00	0.045	0.045	0.044	0.062	0.047	0.072	0.035	1.01	0.99	1.37	1.04	1.61	0.78
	11:00	0.080	0.079	0.078	0.111	0.080	0.132	0.065	0.99	0.97	1.38	1.01	1.65	0.81
	12:00	0.251	0.249	0.249	0.367	0.248	0.452	0.234	0.99	0.99	1.46	0.99	1.80	0.93
	13:00	0.513	0.518	0.521	0.778	0.511	0.972	0.544	1.01	1.02	1.52	1.00	1.89	1.06
01/04/2016	14:00	0.629	0.627	0.634	0.958	0.615	1.208	0.677	1.00	1.01	1.52	0.98	1.92	1.08
	15:00	0.667	0.663	0.671	1.016	0.650	1.284	0.722	0.99	1.01	1.52	0.97	1.93	1.08
	16:00	0.657	0.646	0.653	0.988	0.633	1.247	0.701	0.98	0.99	1.50	0.96	1.90	1.07
	17:00	0.334	0.331	0.332	0.491	0.328	0.608	0.324	0.99	0.99	1.47	0.98	1.82	0.97
	18:00	0.188	0.201	0.201	0.295	0.201	0.362	0.184	1.07	1.07	1.57	1.07	1.93	0.98
	19:00	0.093	0.099	0.098	0.139	0.100	0.167	0.083	1.06	1.05	1.50	1.07	1.80	0.89
	9:00	0.012	0.013	0.012	0.017	0.013	0.019	0.009	1.06	1.03	1.40	1.11	1.60	0.75
	10:00	0.080	0.081	0.080	0.117	0.081	0.142	0.069	1.01	1.00	1.46	1.01	1.78	0.86
	11:00	0.269	0.265	0.267	0.405	0.259	0.512	0.260	0.98	0.99	1.51	0.96	1.90	0.97
	12:00	0.522	0.512	0.520	0.796	0.498	1.017	0.558	0.98	1.00	1.52	0.95	1.95	1.07
	13:00	0.673	0.661	0.675	1.048	0.638	1.356	0.748	0.98	1.00	1.56	0.95	2.02	1.11
02/04/2016	14:00	0.713	0.695	0.709	1.101	0.670	1.425	0.793	0.97	0.99	1.54	0.94	2.00	1.11
	15:00	0.754	0.745	0.760	1.181	0.719	1.529	0.863	0.99	1.01	1.57	0.95	2.03	1.14
	16:00	0.653	0.636	0.649	1.006	0.614	1.300	0.715	0.97	0.99	1.54	0.94	1.99	1.10
	17:00	0.305	0.296	0.299	0.453	0.289	0.573	0.295	0.97	0.98	1.48	0.95	1.88	0.97
	18:00	0.273	0.271	0.274	0.415	0.266	0.525	0.268	0.99	1.00	1.52	0.97	1.92	0.98
	19:00	0.132	0.132	0.132	0.196	0.131	0.243	0.119	1.00	1.00	1.48	0.99	1.84	0.90

Table 6. *Cont.*

	9:00	0.011	0.012	0.012	0.016	0.013	0.019	0.009	1.08	1.10	1.50	1.18	1.72	0.80
	10:00	0.086	0.085	0.089	0.131	0.089	0.161	0.076	0.99	1.03	1.52	1.03	1.87	0.89
	11:00	0.174	0.171	0.179	0.267	0.177	0.332	0.168	0.98	1.03	1.53	1.02	1.91	0.96
	12:00	0.539	0.504	0.535	0.824	0.509	1.059	0.576	0.93	0.99	1.53	0.94	1.96	1.07
	13:00	0.649	0.638	0.676	1.041	0.646	1.336	0.766	0.98	1.04	1.60	0.99	2.06	1.18
03/02/2017	14:00	0.739	0.722	0.766	1.178	0.731	1.510	0.893	0.98	1.04	1.59	0.99	2.04	1.21
	15:00	0.720	0.678	0.718	1.100	0.687	1.407	0.830	0.94	1.00	1.53	0.95	1.95	1.15
	16:00	0.571	0.549	0.584	0.906	0.553	1.171	0.632	0.96	1.02	1.59	0.97	2.05	1.11
	17:00	0.311	0.315	0.334	0.514	0.319	0.659	0.331	1.01	1.08	1.65	1.03	2.12	1.07
	18:00	0.108	0.103	0.107	0.158	0.106	0.196	0.094	0.95	0.99	1.47	0.99	1.81	0.87
	19:00	0.054	0.055	0.057	0.083	0.058	0.101	0.047	1.02	1.06	1.54	1.07	1.86	0.88
	9:00	0.012	0.013	0.012	0.017	0.013	0.019	0.009	1.05	1.04	1.41	1.11	1.62	0.76
	10:00	0.088	0.094	0.096	0.141	0.095	0.173	0.083	1.07	1.09	1.60	1.08	1.97	0.94
	11:00	0.354	0.352	0.363	0.557	0.347	0.713	0.365	1.00	1.02	1.57	0.98	2.01	1.03
	12:00	0.513	0.497	0.513	0.791	0.488	1.018	0.545	0.97	1.00	1.54	0.95	1.98	1.06
	13:00	0.670	0.668	0.691	1.076	0.652	1.397	0.765	1.00	1.03	1.61	0.97	2.08	1.14
16/02/2017	14:00	0.745	0.735	0.760	1.179	0.719	1.524	0.864	0.99	1.02	1.58	0.97	2.05	1.16
	15:00	0.650	0.656	0.677	1.046	0.643	1.347	0.756	1.01	1.04	1.61	0.99	2.07	1.16
	16:00	0.504	0.489	0.504	0.781	0.479	1.007	0.532	0.97	1.00	1.55	0.95	2.00	1.06
	17:00	0.262	0.260	0.267	0.408	0.257	0.520	0.258	0.99	1.02	1.56	0.98	1.99	0.98
	18:00	0.114	0.112	0.114	0.168	0.113	0.207	0.100	0.98	1.00	1.47	0.99	1.82	0.88
	19:00	0.071	0.072	0.072	0.105	0.073	0.128	0.061	1.01	1.02	1.48	1.03	1.80	0.86

Table 6. *Cont.*

	9:00	0.005	0.005	0.005	0.006	0.005	0.006	0.003	0.96	0.90	1.16	1.03	1.26	0.61
	10:00	0.022	0.023	0.022	0.031	0.023	0.036	0.017	1.04	1.01	1.40	1.06	1.63	0.77
	11:00	0.105	0.106	0.105	0.154	0.104	0.190	0.092	1.01	1.00	1.47	0.99	1.81	0.88
	12:00	0.404	0.403	0.406	0.626	0.387	0.804	0.414	1.00	1.01	1.55	0.96	1.99	1.03
	13:00	0.750	0.740	0.748	1.161	0.708	1.501	0.847	0.99	1.00	1.55	0.94	2.00	1.13
26/02/2017	14:00	0.885	0.866	0.875	1.359	0.828	1.758	1.026	0.98	0.99	1.54	0.94	1.99	1.16
	15:00	0.775	0.765	0.773	1.197	0.734	1.544	0.887	0.99	1.00	1.54	0.95	1.99	1.14
	16:00	0.599	0.598	0.606	0.945	0.570	1.229	0.649	1.00	1.01	1.58	0.95	2.05	1.08
	17:00	0.231	0.229	0.229	0.348	0.222	0.441	0.218	0.99	0.99	1.51	0.96	1.91	0.94
	18:00	0.112	0.112	0.111	0.164	0.110	0.203	0.098	1.00	0.99	1.46	0.98	1.81	0.87
	19:00	0.071	0.072	0.071	0.103	0.072	0.126	0.060	1.01	1.00	1.45	1.01	1.77	0.84
	STD								0.031	0.032	0.079	0.054	0.161	0.142
	Mean								0.994	1.013	1.519	0.993	1.906	0.992
	CoV								3.1%	3.1%	5.2%	5.4%	8.5%	14.3%

Note: M_{exp} represents the measured HYSS values (L/m^2·h), whereas $M_{regression}$, M_{Clark}, $M_{Kumar\ and\ Tiwari}$, M_{Dunkle}, M_{PSO}, and $M_{developed\ PSO\ (this\ study)}$ refer to HYSS values predicted by the regression, Clark's, Kumar and Tiwari's, Dunkle's, PSO–HYSS, and the developed PSO–HYSS models, respectively (L/m^2·h).

The predicted results of the regression models, Clark, Kumar and Tiwari, Dunkle's, PSO–HYSS, and the developed PSO–HYSS are compared in Figures 3 and 4. The predicted and estimated HYSS values of different models (regression, Clark, Kumar and Tiwari, Dunkle's, PSO–HYSS, and the developed PSO–HYSS) are compared (Figure 3). The value of R^2 for the developed PSO–HYSS model is the highest, followed by the R^2 value of PSO–HYSS model, then the value of R^2 for the regression model, and so on. Subsequently, the same models' predicted and measured HYSS values are compared (Figure 4). The estimated yield of the developed PSO–HYSS model is nearer to the experimentally measured yield compared with other models.
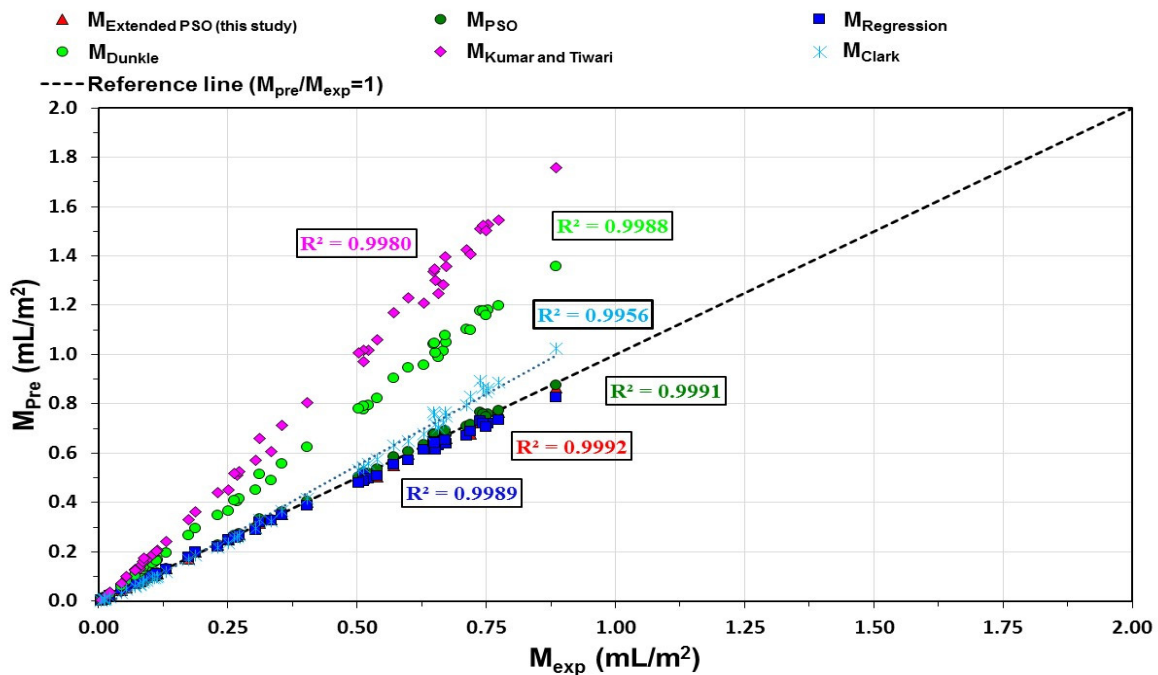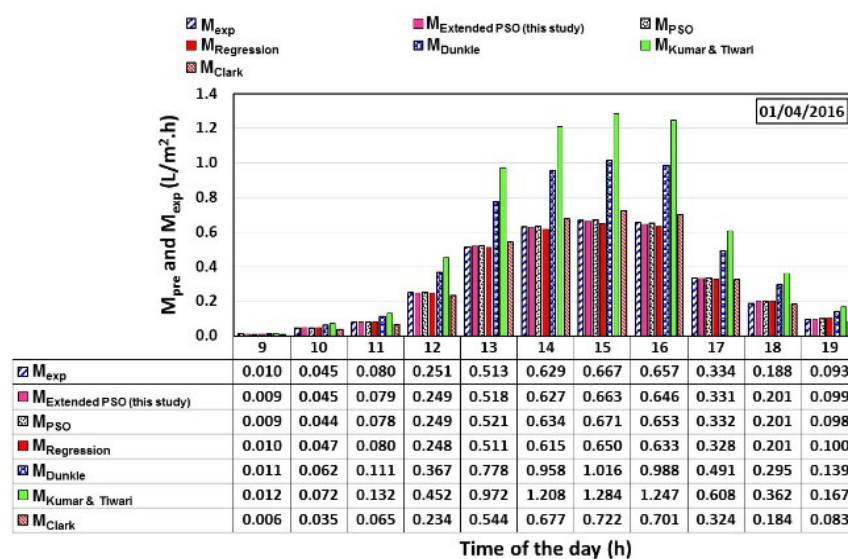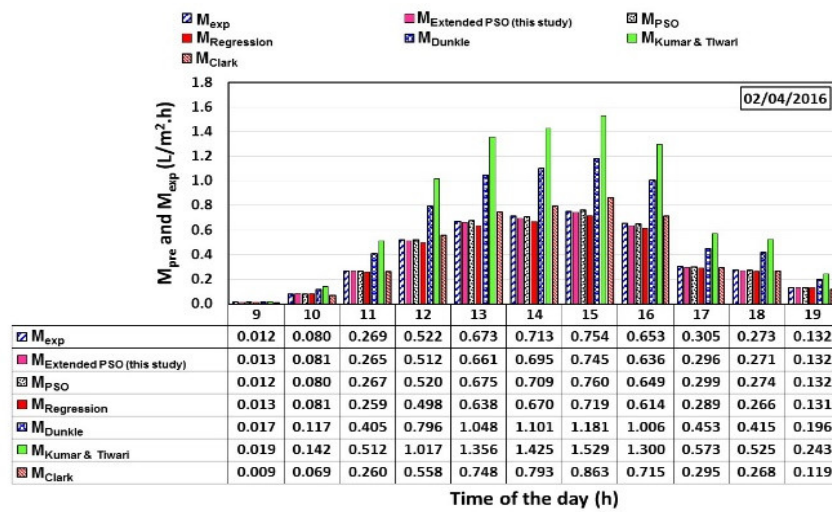

Figure 3. Hourly yield predictions versus hourly measurement (experimental) data by regression, Clark's, Kumar and Tiwari's, Dunkle's, PSO–HYSS, and the developed PSO–HYSS models.
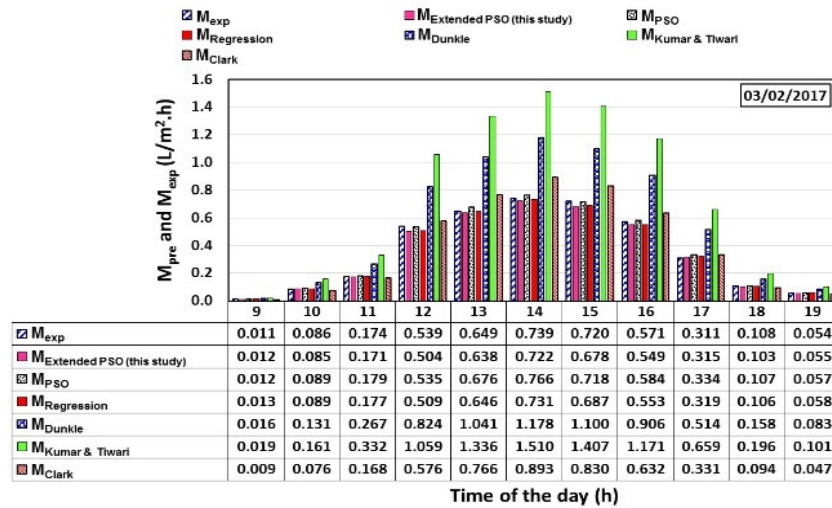

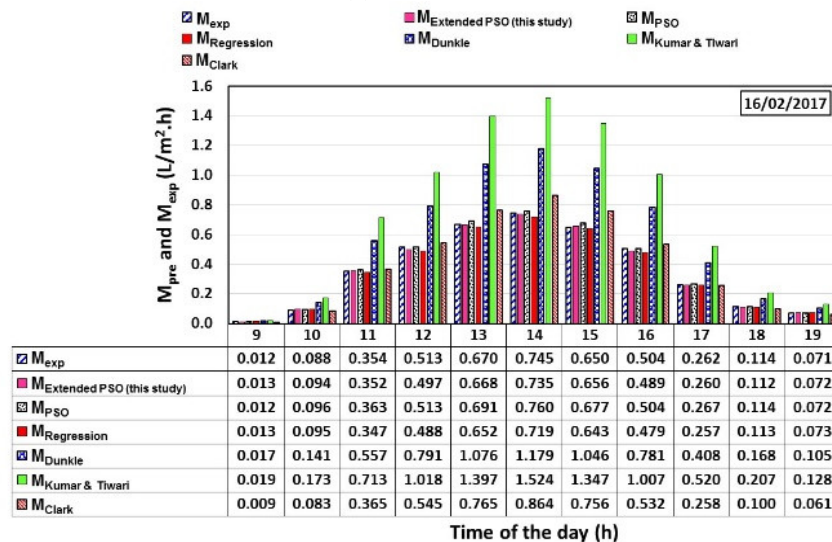|	9	10	11	12	13	14	15	16	17	18	19
M_{exp}	0.010	0.045	0.080	0.251	0.513	0.629	0.667	0.657	0.334	0.188	0.093
$M_{Extended\ PSO\ (this\ study)}$	0.009	0.045	0.079	0.249	0.518	0.627	0.663	0.646	0.331	0.201	0.099
M_{PSO}	0.009	0.044	0.078	0.249	0.521	0.634	0.671	0.653	0.332	0.201	0.098
$M_{Regression}$	0.010	0.047	0.080	0.248	0.511	0.615	0.650	0.633	0.328	0.201	0.100
M_{Dunkle}	0.011	0.062	0.111	0.367	0.778	0.958	1.016	0.988	0.491	0.295	0.139
$M_{Kumar\ \&\ Tiwari}$	0.012	0.072	0.132	0.452	0.972	1.208	1.284	1.247	0.608	0.362	0.167
M_{Clark}	0.006	0.035	0.065	0.234	0.544	0.677	0.722	0.701	0.324	0.184	0.083

(**a**) 01-04-2016

Figure 4. *Cont.*

	M_exp			
	M_Extended PSO (this study)		M_PSO	
	M_Regression		M_Dunkle	
	M_Clark		M_Kumar & Tiwari	

02/04/2016

	9	10	11	12	13	14	15	16	17	18	19
M_{exp}	0.012	0.080	0.269	0.522	0.673	0.713	0.754	0.653	0.305	0.273	0.132
$M_{Extended\ PSO\ (this\ study)}$	0.013	0.081	0.265	0.512	0.661	0.695	0.745	0.636	0.296	0.271	0.132
M_{PSO}	0.012	0.080	0.267	0.520	0.675	0.709	0.760	0.649	0.299	0.274	0.132
$M_{Regression}$	0.013	0.081	0.259	0.498	0.638	0.670	0.719	0.614	0.289	0.266	0.131
M_{Dunkle}	0.017	0.117	0.405	0.796	1.048	1.101	1.181	1.006	0.453	0.415	0.196
$M_{Kumar\ \&\ Tiwari}$	0.019	0.142	0.512	1.017	1.356	1.425	1.529	1.300	0.573	0.525	0.243
M_{Clark}	0.009	0.069	0.260	0.558	0.748	0.793	0.863	0.715	0.295	0.268	0.119

Time of the day (h)

(**b**) 02-04-2016

	M_exp			
	M_Extended PSO (this study)		M_PSO	
	M_Regression		M_Dunkle	
	M_Clark		M_Kumar & Tiwari	

03/02/2017

	9	10	11	12	13	14	15	16	17	18	19
M_{exp}	0.011	0.086	0.174	0.539	0.649	0.739	0.720	0.571	0.311	0.108	0.054
$M_{Extended\ PSO\ (this\ study)}$	0.012	0.085	0.171	0.504	0.638	0.722	0.678	0.549	0.315	0.103	0.055
M_{PSO}	0.012	0.089	0.179	0.535	0.676	0.766	0.718	0.584	0.334	0.107	0.057
$M_{Regression}$	0.013	0.089	0.177	0.509	0.646	0.731	0.687	0.553	0.319	0.106	0.058
M_{Dunkle}	0.016	0.131	0.267	0.824	1.041	1.178	1.100	0.906	0.514	0.158	0.083
$M_{Kumar\ \&\ Tiwari}$	0.019	0.161	0.332	1.059	1.336	1.510	1.407	1.171	0.659	0.196	0.101
M_{Clark}	0.009	0.076	0.168	0.576	0.766	0.893	0.830	0.632	0.331	0.094	0.047

Time of the day (h)

(**c**) 03-02-2017

	M_exp			
	M_Extended PSO (this study)		M_PSO	
	M_Regression		M_Dunkle	
	M_Clark		M_Kumar & Tiwari	

16/02/2017

	9	10	11	12	13	14	15	16	17	18	19
M_{exp}	0.012	0.088	0.354	0.513	0.670	0.745	0.650	0.504	0.262	0.114	0.071
$M_{Extended\ PSO\ (this\ study)}$	0.013	0.094	0.352	0.497	0.668	0.735	0.656	0.489	0.260	0.112	0.072
M_{PSO}	0.012	0.096	0.363	0.513	0.691	0.760	0.677	0.504	0.267	0.114	0.072
$M_{Regression}$	0.013	0.095	0.347	0.488	0.652	0.719	0.643	0.479	0.257	0.113	0.073
M_{Dunkle}	0.017	0.141	0.557	0.791	1.076	1.179	1.046	0.781	0.408	0.168	0.105
$M_{Kumar\ \&\ Tiwari}$	0.019	0.173	0.713	1.018	1.397	1.524	1.347	1.007	0.520	0.207	0.128
M_{Clark}	0.009	0.083	0.365	0.545	0.765	0.864	0.756	0.532	0.258	0.100	0.061

Time of the day (h)

(**d**) 16-02-2017

Figure 4. *Cont.*

(**e**) 26-02-2017

Figure 4. Comparison of the experimentally measured values with the predicted values from the regression models, Clark, Kumar and Tiwari, Dunkle's, PSO–HYSS, and the developed PSO–HYSS.

Figures 3 and 4 indicate the reliability and accuracy of the developed PSO–HYSS model. Mean value of the developed PSO–HYSS model that is equal to 0.994 is the nearer to 1.0 than that of the PSO–HYSS model that is equal to 1.013, Dunkle's model which is equal to 1.519, Kumar and Tiwari's model that is equal to 1.906, Clark's model that is equal to 0.992, and regression model that is equal to 0.993. Furthermore, the value of the *CoV* of the developed PSO–HYSS model that equals to 3.10 percent, which is same to the one related to the PSO–HYSS model, is more consistent and accurate than those of Dunkle's model that is equal to 5.2 percent, Kumar and Tiwari's model which is equal to 8.5 percent, Clark's model that is equal to 14.3 percent, and regression model that is equal to 5.4 percent. The *CoV* result shows a high prediction accuracy of the developed PSO–HYSS model [75]. Moreover, the R^2 of the developed PSO–HYSS model is 0.9992, which is also better than those of the other models.

The developed PSO–HYSS model gave an excellent correlation between the estimated and the measured values of the HYSS. Thus, the developed PSO–HYSS model can be used to estimate the HYSS efficiently. Statistical analysis is carried using *PI*, *R*, and *RRMSE* to inspect the efficiency of the developed PSO–HYSS model (Equations (28)–(30)). The statistical interpretation of the regression models, Clark, Kumar and Tiwari, Dunkle's, PSO–HYSS, and the developed PSO–HYSS is illustrated in Table 7.

Table 7. *R*, *PI*, and *RRMSE* of regression, Kumar and Tiwari's, Clark's, Dunkle's, PSO–HYSS, and the developed PSO–HYSS models.

Model	Predicted Versus Experimental		
	R	*PI*	*RRMSE* (%)
Regression	0.9989	0.0308	6.15
Kumar and Tiwari's	0.9980	0.7072	141.37
Clark's	0.9956	0.0891	17.81
Dunkle's	0.9988	0.3935	78.68
PSO-HYSS	0.9991	0.0173	3.46
Developed PSO-HYSS (this study)	0.9992	0.0141	2.81

The *R* value obtained for the developed PSO–HYSS model (0.9992), PSO–HYSS model (0.9991), and regression model (0.9989) are higher than the ones obtained for Dunkle's and

Kumar and Tiwari's models. In addition, the *RRMSE* values of the developed PSO–HYSS, PSO–HYSS, and regression models are lower than those of the other models. Findings indicate that these models can predict the HYSS with high accuracy. Generally, a low RRMSE value such as that of the developed PSO–HYSS model (2.81) suggests that the model can accurately predict hourly yields. By contrast, a high *RRMSE* value such as those for Dunkle's model (78.68) and Kumar and Tiwari's model (141.37) indicates low degrees of accuracy in predicted yields. Clark's model obtains a mild value of *RRMSE* (17.81); thus, this model has a medium degree of accuracy in predicting the HYSS.

R and *RRMSE* are two important parameters used to evaluate the HYSS prediction models for DSSSHS. Using those two parameters, the developed PSO–HYSS model obtains the lowest value of *RRMSE* and the highest value of *R*. Therefore, all of the other forecasting models are overcome by the developed PSO–HYSS model. Another indicative parameter (PI) is also used to assess the accuracy of prediction models. Table 7 illustrates that the developed PSO–HYSS model has a *PI* value equal to 0.0141 that is located within the acceptable limit (*PI* less than 0.1). The value of *PI* for the PSO–HYSS model is also less than those of Clark's model which is equal to 0.0891, regression model to 0.0308, and PSO–HYSS model is equal to 0.0173. Thus, we can say that the developed PSO–HYSS model is the best when compared with the regression, Clark's, and PSO–HYSS models in terms of covariance, correlation, and acceptability of the *PI* level. The *PI* values of Kumar and Tiwari's model equal to 0.7072 and Dunkle's model equal to 0.3935 are both beyond acceptable limits; thus, those models display low accuracy in forecasting the HYSS of DSSSHS. The result of the external validation of the regression, Kumar and Tiwari's, Clark's, Dunkle's, PSO–HYSS, and the developed PSO–HYSS models are all illustrated in Table 8.

Table 8. Statistical parameters for external validation of regression, Kumar and Tiwari's, Clark's, Dunkle's, PSO–HYSS, and the developed PSO–HYSS models.

Item	Formulas	Conditions	Developed PSO–HYSS (Current Study)	PSO–HYSS	Regression	Dunkle's	Kumar and Tiwari's	Clark's
1	R, Equation (30)	R more than 0.8	0.9992	0.9991	0.9989	0.9988	0.9980	0.9956
	$k = \frac{\sum_{i=1}^{NS}(y \times \acute{y})}{y^2}$	$0.85 < k < 1.15$	0.9830	1.0084	0.962	1.552	1.992	1.110
3	$k' = \frac{\sum_{i=1}^{NS}(y \times \acute{y})}{\acute{y}^2}$	$0.85 < k' < 1.15$	1.0170	0.9914	1.039	0.644	0.501	0.899
4	$R_m = R^2 \times \left(1 - \sqrt{|R^2 - Ro^2|}\right)$	R_m more than 0.5	0.9957	0.9727	0.944	0.413	0.178	0.843
5	$mp = \frac{(R^2 - Ro^2)}{R^2}$	$|mp|$ less than 0.1	0.00000	−0.00071	0.00288	0.81633	2.59689	0.02558
6	$np = \frac{(R^2 - Ro'^2)}{R^2}$	$|np|$ lass than 0.1	−0.00001	−0.00070	0.00300	0.34419	0.67563	0.02372

4.3. Effects of Solar Radiation and NSM on the Productivity of Solar Still

The effects of solar radiation on the solar still's yield are measured with various *NSMs* and water depths. The relation of the 24 experiments implemented for the DSSSHS between the daily water production and the daily solar radiation is shown in Figure 5a. For all *NSMs* and water depths, the DSSSHS daily experimental yield values are directly proportional to the daily solar radiation.

As shown in Figure 5a, we can notice that the daily yield of the DSSSHS is directly proportional to *NSM* for the same salty water depth values and under the same daily solar radiation. In other words, the daily yield increases with the rise of the NSM for the same salty water depth values and under the same day solar radiation. However, the yield increase eventually decreases significantly after *NSM* = 6. These results are consistent with the findings of [26,38,76–83]. These studies concluded that efficiency is directly proportional to the amount of solar radiation the solar still receives.
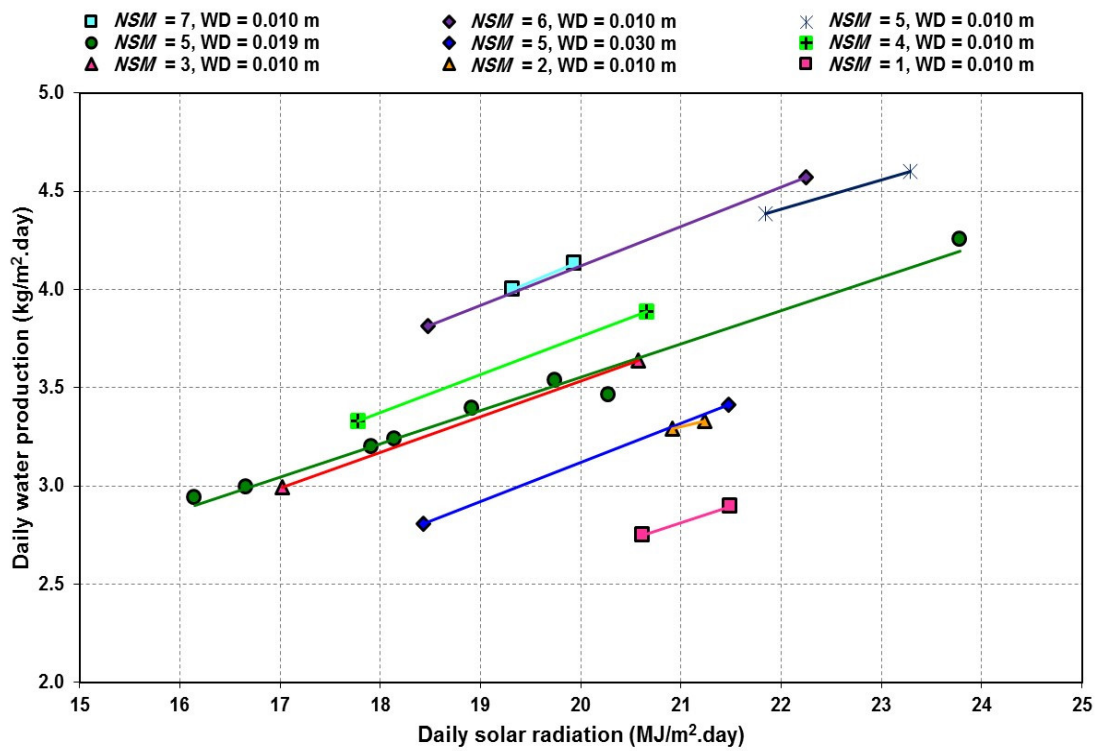
(a)
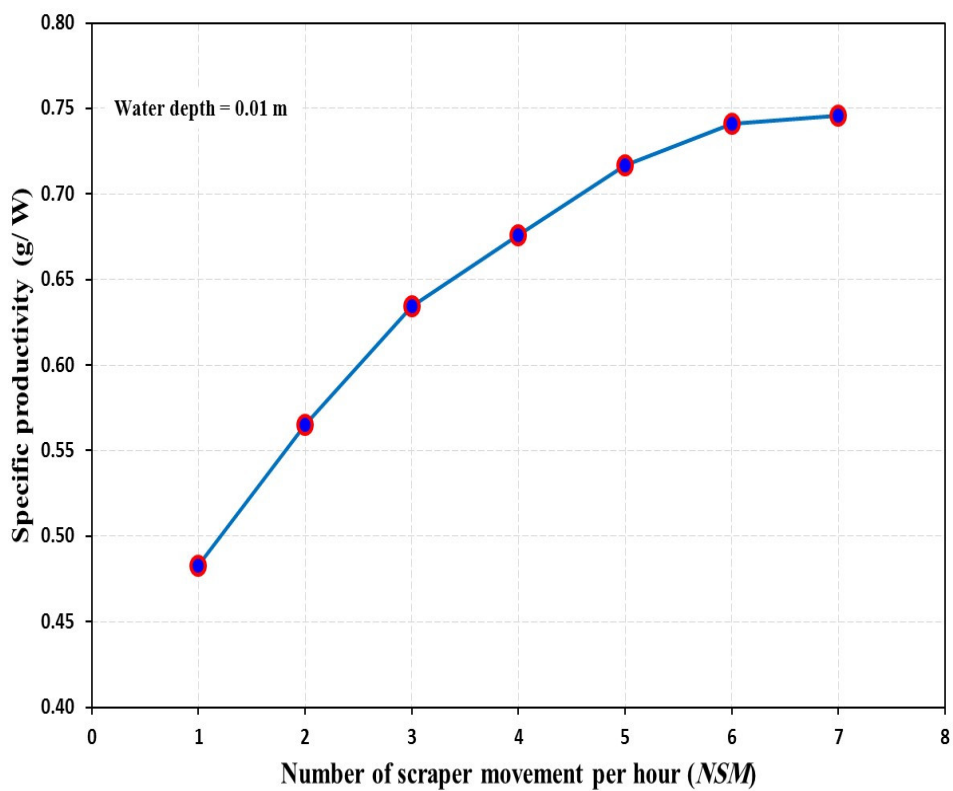
(b)

Figure 5. *Cont.*

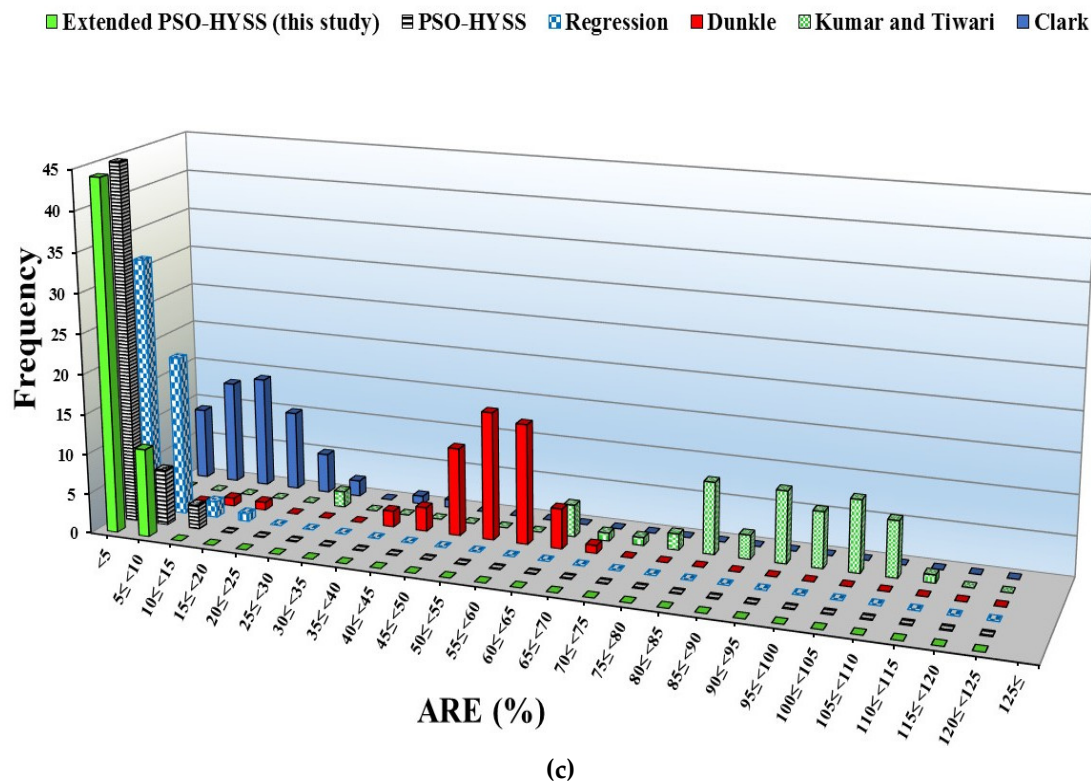**Figure 5.** (**a**) Daily production versus daily solar radiation of DSSSHS with different water depths and NSMs, (**b**) Variations of the specific productivity of DSSSHS with various NSM and fixed water depth = 0.01 m, (**c**) ARE distribution of regression, Kumar and Tiwari's, Clark's, Dunkle's, PSO–HYSS, and the developed PSO–HYSS models.

These observations can produce a powerful tool for comparing the interpretation of DSSSHS with various NSMs still's productivity per unit solar radiation with different *NSMs*, that is, the specific productivities of the solar still with different *NSMs* [84]. Variations in the specific productivity of the DSSSHS with different *NSMs* at a fixed salty water depth of 0.01 m are presented in Figure 5b. The specific productivity of the DSSSHS is directly proportional to *NSM*; that is, increasing the *NSM* also increases specific productivity. Results show that for *NSMs* equal to 7, 6, 5, 4, 3, 2, and 1 the specific productivities are 0.746, 0.741, 0.717, 0.676, 0.635, 0.565, and 0.483 g/W, respectively.

4.4. Error Analysis

The percentage of absolute relative error (*ARE*) is utilized to assess the error between predicted and experimental data. Then, the model's predicting abilities are compared based on the distribution of *ARE* [85]. Thus, the percentage of the *ARE* can be calculated using the following equation [86]:

$$ARE = \left| \frac{y - \acute{y}}{y} \right| \times 100. \tag{33}$$

ARE distributions for Kumar and Tiwari's, Clark's, regression, Dunkle's, PSO–HYSS, and the developed PSO–HYSS models are shown in Figure 5c. Typically, the frequency decreases as *ARE* increases. Figure 5c reveals the high frequency of the minimal *ARE* < 5% attained by the developed PSO-HYSS model, whereas the low frequency reported the highest *ARE* >10%. On the other hand, regression model indicated high frequency with minimal *ARE* < 5%, whereas the low frequency attained high *ARE* ≥ 20%. Clark's model achieves moderate frequencies with low *ARE* (<5%) and the lowest frequencies with high *ARE* (≥45%).

Regarding appropriate error distribution, the established PSO–HYSS model is followed by the PSO–HYSS model, and then the regression model. Clark's model achieves a moderately acceptable distribution of errors. Dunkle's and Kumar and Tiwari's models obtain the lowest frequencies with low *AREs* (<5%) and high frequencies with high *AREs*, namely 70% > $ARE \geq 35\%$ and 115% > $ARE \geq 60\%$, respectively. Overall findings indicate an impermissible error distribution. Nonetheless, the developed PSO–HYSS model is the best compared with other forecasting models in terms of error prediction.

4.5. Uncertainty Analysis

Total uncertainty of the measurements can be calculated in each measurement by combining the accuracies of the measuring sensor and instrument. However, the worse value for the uncertainty may be yielded if the personal errors of the sensor and measuring devices are simply added. Square root sum is calculated, an improved and more realistic approach to calculating total accuracy [87].

$$\delta_{total} = \sqrt{(\delta_{sensor})^2 + (\delta_{instrument})^2}, \tag{34}$$

where $\delta_{instrument}$, δ_{sensor}, and δ_{total} are the measuring instrument, sensor, and total accuracies, respectively.

Equation (34) is used for estimating the measurement uncertainties and applying the instruments' accuracies listed in Table 4. The highest percentages of the uncertainties for the measured values of temperature, yield, and solar radiation measured using thermocouples, electronic balance, and pyranometer are $\pm 0.60\%$, $\pm 2.00\%$, and $\pm 2.01\%$, respectively.

4.6. Discussion

In this study, two hundred sixty-two sets of data are collected for twenty-four days for various *NSM*, depths of salty water, and climatic conditions for the same east-west orientation. Those data sets are utilized for building and validating the proposed PSO–HYSS model for DSSSHS. Results showed that the optimized values of *f*, *z*, *n*, and *C*, which represent the unknown constants in the improved model, enhance the accuracy of estimating HYSS. For the verification of the developed model, its predicted values of the HYSS are compared with the estimated yields acquired by the regression model [39], PSO–HYSS model [45], and others [40,47]. Comparison results confirmed the reliability of the developed PSO–HYSS model which provides more accurate and consistent results than the abovementioned extant models. The newly developed PSO–HYSS model in this research uses an accurate optimization model, that is, PSO, and integrates the effect of NSM on HYSS in the prediction model for the first time. This suggested method is based on determining *f*, *z*, *n*, and *C* values, which are the unknown constants in the model used to estimate HYSS. Regarding the model accuracy, the PSO–HYSS model demonstrated high accuracy and trustworthy technology that can be practiced in reliable applications.

5. Conclusions

In this research, different numbers of scraper motions per hour (1, 2, 3, 4, 5, 6, and 7) were implemented to increase the productivity of solar still (HYSS) of double-slope solar still hybrid with rubber scrapers (DSSSHS) in areas of low latitude. The investigation was conducted to further develop an accurate model for HYSS prediction. The suggested model is based on determining the best values for the unknown constants *f*, *z*, *n*, and *C* by obtaining the optimum values of these constants using the PSO algorithm. Those constants are subsequently used to build the hourly yield prediction model. Predicted yield values were validated against the actual experiments. For verifying the reliability of the newly developed model, the predicted values were compared with those calculated by the models of regression, Dunkle's, PSO–HYSS, Clark, and Kumar and Tiwari. The conclusions of the current research were summarized as follows:

■   *NSM* revealed a significant effect on DSSSHS productivity and HYSS prediction accuracy.

- ■　The specific productivity of the DSSSHS with a fixed water depth of 0.01 m is directly proportional to the magnitude of *NSM*, in which the specific productivity increases with *NSM*. To inspect the impacts of *NSM* on the predicted yield accuracy of DSSSHS, an improved PSO–HYSS was developed with consideration of the effects of *NSM*. Comparing the predicted and measured value results indicated that the PSO–HYSS model gave the superior predictability performance yields with the other models. Thus, the proposed model was confirmed to be effective and efficient for the prediction process.

- ■　By validating the results of the error analysis, PSO-HYSS attained the lower frequency "*ARE* ≥ 10%" and high frequency at low "*ARE* < 5%". Models within the spectrum of acceptable error distribution may be ordered as follows: developed PSO–HYSS, regression, and Clark's. Thus, in terms of error prediction, the developed PSO–HYSS model can be considered the best among other models.

- ■　Statistical analysis indicated a consistent results for the developed PSO-HYSS model.

Appendix A. Flowchart of Developed PSO–HYSS Model for HYSS Estimation
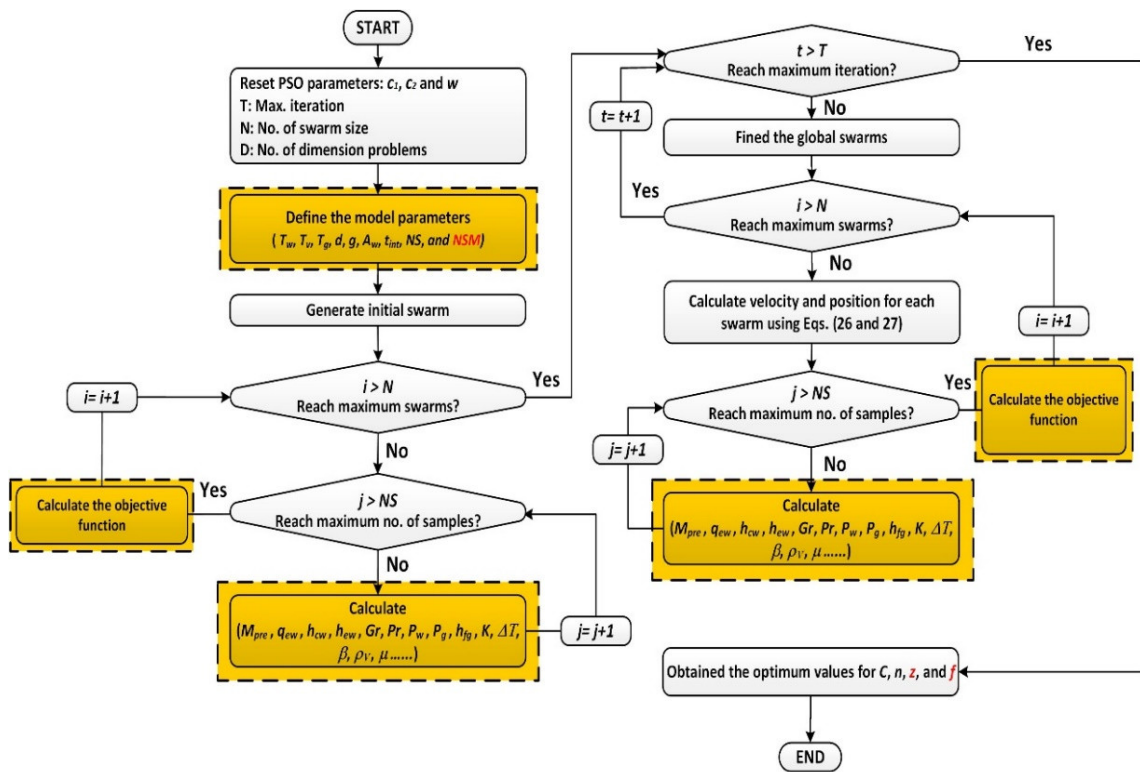
Appendix B. Isometric Diagram of DSSSHS
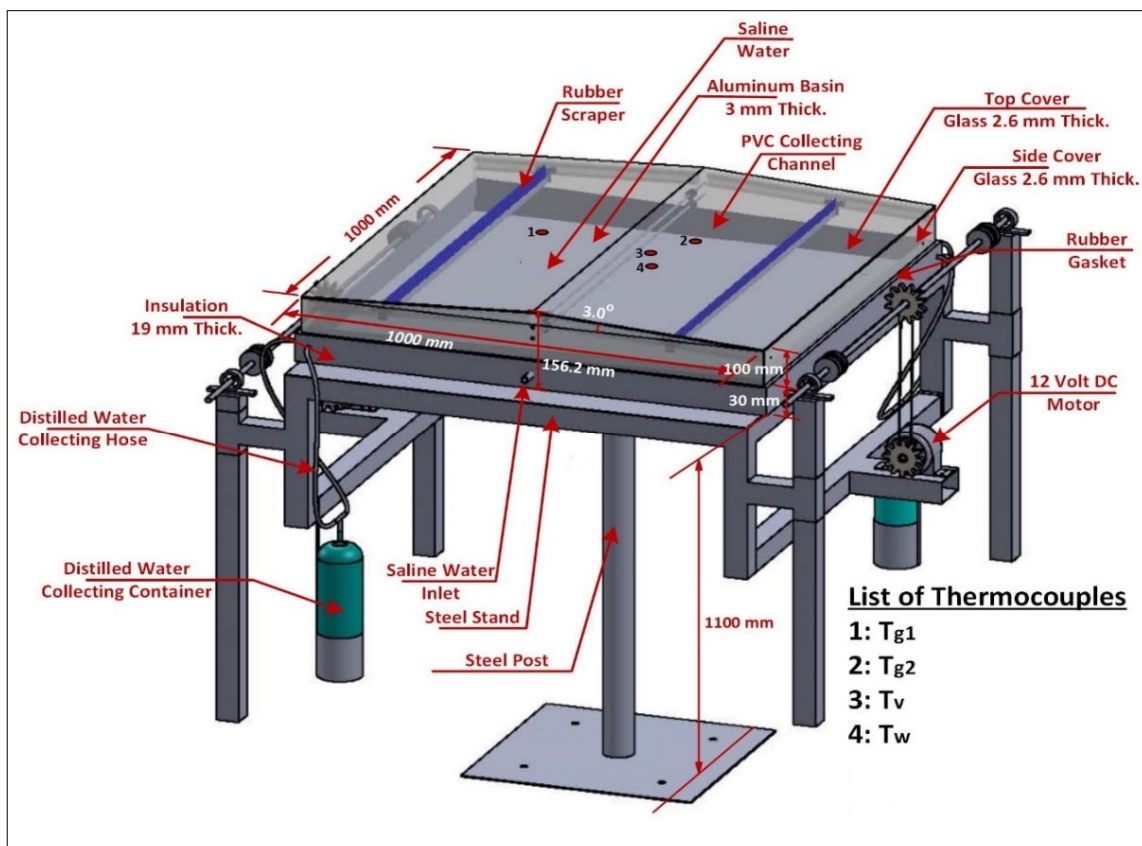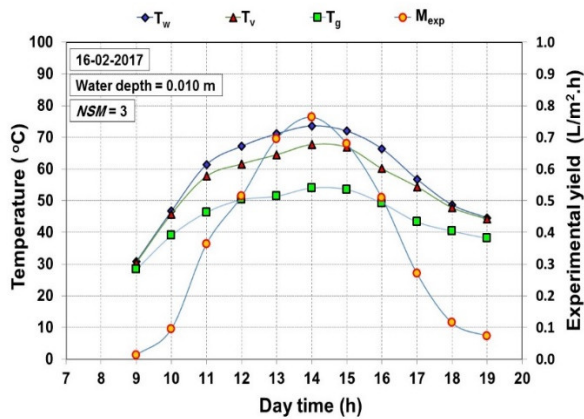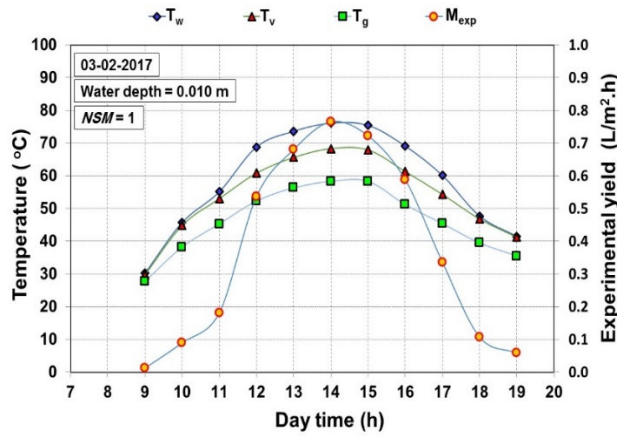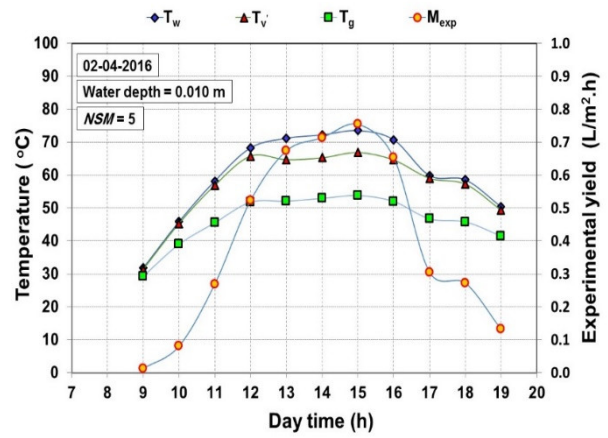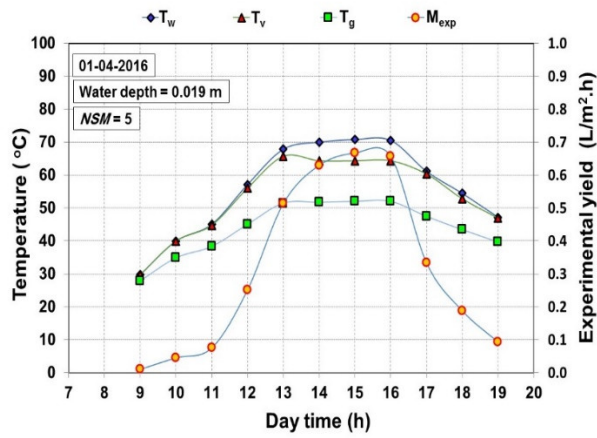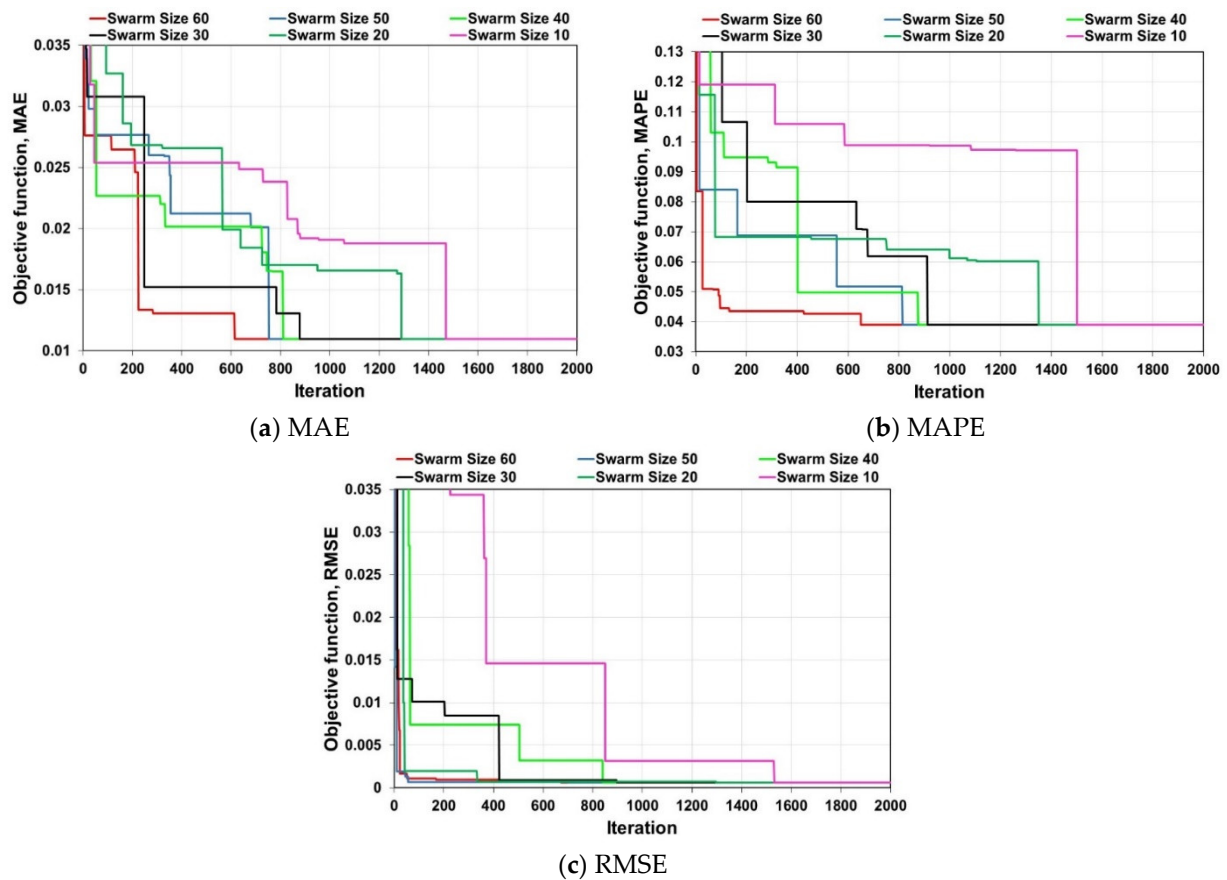
Appendix C. Experimental Records of 207 Datasets (19 days) for Developed PSO–HYSS Model Construction. Note: NSM Is the Number of Scraper Motions per Hour
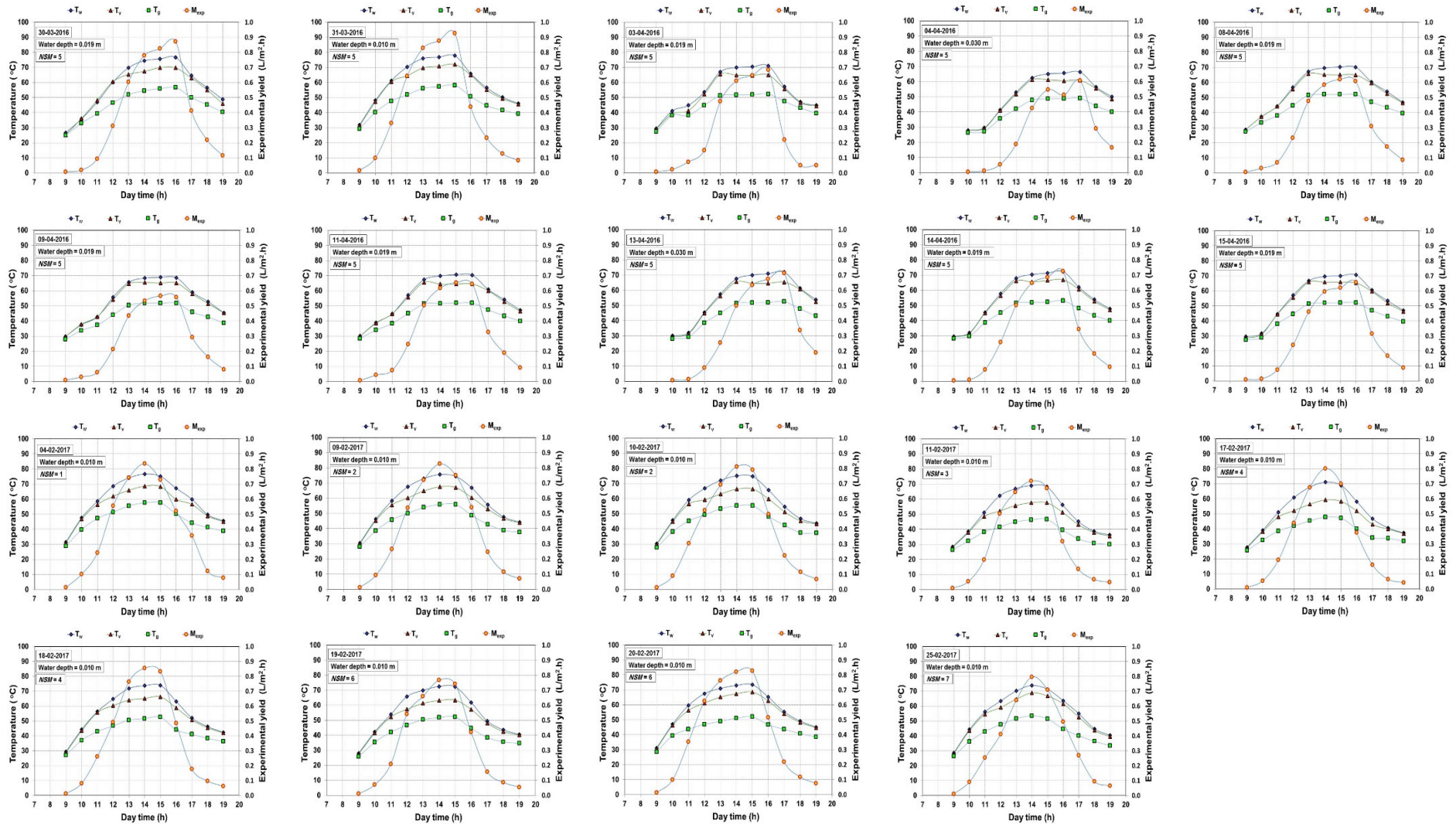
Appendix D. Experimental Records of Fifty-Five Datasets for the Developed PSO–HYSS Model Verification
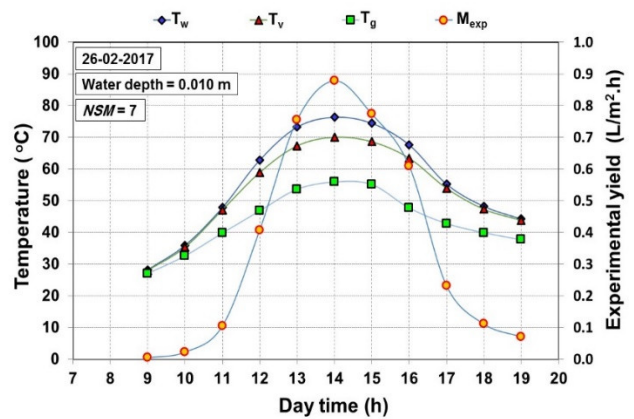
Appendix E. Convergence of Different Swarm Sizes Used in Developed PSO–HYSS Model

(**a**) MAE

(**b**) MAPE

(**c**) RMSE

References

1. Khawaji, A.D.; Kutubkhanah, I.K.; Wie, J.-M. Advances in seawater desalination technologies. *Desalination* **2008**, *221*, 47–69. [CrossRef]
2. Kabeel, A.E. Performance of solar still with a concave wick evaporation surface. *Energy* **2009**, *34*, 1504–1509. [CrossRef]
3. Dev, R.; Tiwari, G.N. Characteristic equation of the inverted absorber solar still. *Desalination* **2011**, *269*, 67–77. [CrossRef]
4. Abu-Arabi, M.; Zurigat, Y.; Al-Hinai, H.; Al-Hiddabi, S. Modeling and performance analysis of a solar desalination unit with double-glass cover cooling. *Desalination* **2002**, *143*, 173–182. [CrossRef]
5. Arunkumar, T.; Jayaprakash, R.; Ahsan, A.; Denkenberger, D.; Okundamiya, M.S. Effect of water and air flow on concentric tubular solar water desalting system. *Appl. Energy* **2013**, *103*, 109–115. [CrossRef]
6. Kabeel, A.E.; Khairat Dawood, M.M.; Ramzy, K.; Nabil, T.; Elnaghi, B.; Elkassar, A. Enhancement of single solar still integrated with solar dishes: An experimental approach. *Energy Convers. Manag.* **2019**, *196*, 165–174. [CrossRef]
7. Abu-Hijleh, B.A.; Rababa'h, H.M. Experimental study of a solar still with sponge cubes in basin. *Energy Convers. Manag.* **2003**, *44*, 1411–1418. [CrossRef]
8. Alawee, W.H.; Dhahad, H.A.; Ahmed, I.S.; Mohammad, T.A. Experimental investigation on an elevated basin solar still with integrated internal reflectors and inclined fins. *J. Eng. Sci. Technol.* **2021**, *16*, 762–777.
9. Taqi, R.N.; Abdul Redha, Z.A.; Mustafa, F.I. Experimental Investigation of a Single Basin-Single Slope Solar Still Coupled with Evacuated Tube Solar Collector. *J. Eng.* **2021**, *27*, 16–34. [CrossRef]
10. Tabrizi, F.F.; Sharak, A.Z. Experimental study of an integrated basin solar still with a sandy heat reservoir. *Desalination* **2010**, *253*, 195–199. [CrossRef]
11. Al_qasaab, M.R.; Abed, Q.A.; Abd Al-wahid, W.A. Enhancement the Solar Distiller Water By Using Parabolic Dish Collector With Single Slope Solar Still. *J. Therm. Eng.* **2021**, *7*, 1000–1015. [CrossRef]
12. Ahsan, A.; Fukuhara, T. Condensation Mass Transfer in Unsaturated Humid Air Inside Tubular Solar Still. *J. Hydrosci. Hydraul. Eng.* **2010**, *28*, 31–42.
13. Danish, S.N.; El-Leathy, A.; Alata, M.; Al-Ansary, H. Enhancing solar still performance using vacuum pump and geothermal energy. *Energies* **2019**, *12*, 539. [CrossRef]

14. Dumka, P.; Sharma, A.; Kushwah, Y.; Raghav, A.S.; Mishra, D.R. Performance evaluation of single slope solar still augmented with sand-filled cotton bags. *J. Energy Storage* **2019**, *25*, 100888. [CrossRef]

15. Abdel-Rehim, Z.S.; Lasheen, A. Experimental and theoretical study of a solar desalination system located in Cairo, Egypt. *Desalination* **2007**, *217*, 52–64. [CrossRef]

16. Attia, M.E.H.; Driss, Z.; Manokar, A.M.; Sathyamurthy, R. Effect of aluminum balls on the productivity of solar distillate. *J. Energy Storage* **2020**, *30*, 101466. [CrossRef]

17. Esfahani, J.A.; Rahbar, N.; Lavvaf, M. Utilization of thermoelectric cooling in a portable active solar still—An experimental study on winter days. *Desalination* **2011**, *269*, 198–205. [CrossRef]

18. Guo, H.; Tao, H.; Salih, S.Q.; Yaseen, Z.M. Optimized parameter estimation of a PEMFC model based on improved Grass Fibrous Root Optimization Algorithm. *Energy Rep.* **2020**, *6*, 1510–1519. [CrossRef]

19. Ahsan, A.; Syuhada, N.; Jolhi, E.; Darain, K.M.; Rowshon, M.K.; Jakariya, M.; Shafie, S.; Ghazali, A.H. Assessment of distillate water quality parameters produced by solar still for potable usage. *Fresenius Environ. Bull.* **2014**, *23*, 859–866.

20. Sathyamurthy, R.; Nagarajan, P.K.; Subramani, J.; Vijayakumar, D.; Mohammed Ashraf Ali, K. Effect of Water Mass on Triangular Pyramid Solar Still Using Phase Change Material as Storage Medium. *Energy Procedia* **2014**, *61*, 2224–2228. [CrossRef]

21. Velmurugan, V.; Gopalakrishnan, M.; Raghu, R.; Srithar, K. Single basin solar still with fin for enhancing productivity. *Energy Convers. Manag.* **2008**, *49*, 2602–2608. [CrossRef]

22. Arunkumar, T.; Velraj, R.; Ahsan, A.; Khalifa, A.J.N.; Shams, S.; Denkenberger, D.; Sathyamurthy, R. Effect of parabolic solar energy collectors for water distillation. *Desalin. Water Treat.* **2015**, *57*, 21234–21242. [CrossRef]

23. Arunkumar, T.; Velraj, R.; Denkenberger, D.C.; Sathyamurthy, R.; Kumar, K.V.; Ahsan, A. Productivity enhancements of compound parabolic concentrator tubular solar stills. *Renew. Energy* **2016**, *88*, 391–400. [CrossRef]

24. Karimi Estahbanati, M.R.; Ahsan, A.; Feilizadeh, M.; Jafarpur, K.; Ashrafmansouri, S.-S.; Feilizadeh, M. Theoretical and experimental investigation on internal reflectors in a single-slope solar still. *Appl. Energy* **2016**, *165*, 537–547. [CrossRef]

25. Ahsan, A.; Islam, K.M.S.; Fukuhara, T.; Ghazali, A.H. Experimental study on evaporation, condensation and production of a new Tubular Solar Still. *Desalination* **2010**, *260*, 172–179. [CrossRef]

26. Rahbar, N.; Esfahani, J.A.; Asadi, A. An experimental investigation on productivity and performance of a new improved design portable asymmetrical solar still utilizing thermoelectric modules. *Energy Convers. Manag.* **2016**, *118*, 55–62. [CrossRef]

27. Arunkumar, T.; Jayaprakash, R.; Denkenberger, D.; Ahsan, A.; Okundamiya, M.S.; Kumar, S.; Tanaka, H.; Aybar, H.Ş. An experimental study on a hemispherical solar still. *Desalination* **2012**, *286*, 342–348. [CrossRef]

28. Ali, H.M. Experimental study on air motion effect inside the solar still on still performance. *Energy Convers. Manag.* **1991**, *32*, 67–70. [CrossRef]

29. Rashidi, S.; Bovand, M.; Esfahani, J.A. Optimization of partitioning inside a single slope solar still for performance improvement. *Desalination* **2016**, *395*, 79–91. [CrossRef]

30. Kabeel, A.E.; Omara, Z.M.; Essa, F.A. Improving the performance of solar still by using nanofluids and providing vacuum. *Energy Convers. Manag.* **2014**, *86*, 268–274. [CrossRef]

31. Alawee, W.H. Improving the productivity of single effect double slope solar still by modification simple. *J. Eng.* **2015**, *21*, 50–60.

32. Patel, S.K.; Singh, D.; Devnani, G.L.; Sinha, S.; Singh, D. Potable water production via desalination technique using solar still integrated with partial cooling coil condenser. *Sustain. Energy Technol. Assess.* **2021**, *43*, 100927. [CrossRef]

33. Mevada, D.; Panchal, H.; Ahmadein, M.; Zayed, M.E.; Alsaleh, N.A.; Djuansjah, J.; Moustafa, E.B.; Elsheikh, A.H.; Sadasivuni, K.K. Investigation and performance analysis of solar still with energy storage materials: An energy-exergy efficiency analysis. *Case Stud. Therm. Eng.* **2022**, *29*, 101687. [CrossRef]

34. Thalib, M.M.; Manokar, A.M.; Essa, F.A.; Vasimalai, N.; Sathyamurthy, R.; Garcia Marquez, F.P. Comparative Study of Tubular Solar Stills with Phase Change Material and Nano-Enhanced Phase Change Material. *Energies* **2020**, *13*, 3989. [CrossRef]

35. Rashidi, S.; Akar, S.; Bovand, M.; Ellahi, R. Volume of fluid model to simulate the nanofluid flow and entropy generation in a single slope solar still. *Renew. Energy* **2018**, *115*, 400–410.

36. Khalifa, A.J.N. On the effect of cover tilt angle of the simple solar still on its productivity in different seasons and latitudes. *Energy Convers. Manag.* **2011**, *52*, 431–436. [CrossRef]

37. Abdallah, S.; Badran, O.; Abu-Khader, M.M. Performance evaluation of a modified design of a single slope solar still. *Desalination* **2008**, *219*, 222–230.

38. Aybar, H.Ş.; Egelioğlu, F.; Atikol, U. An experimental study on an inclined solar water distillation system. *Desalination* **2005**, *180*, 285–289.

39. Al-Sulttani, A.O.; Ahsan, A.; Rahman, A.; Nik Daud, N.N.; Idrus, S. Heat transfer coefficients and yield analysis of a double-slope solar still hybrid with rubber scrapers: An experimental and theoretical study. *Desalination* **2017**, *407*, 61–74. [CrossRef]

40. Dunkle, R.V. Solar water distillation: The roof type still and a multiple effect diffusion still. In Proceedings of the International Heat Transfer Conference, University of Colorado, Boulder, CO, USA, 28 August–1 September 1961; Volume 5, p. 895.

41. Tsilingiris, P.T. Analysis of the heat and mass transfer processes in solar stills—The validation of a model. *Sol. Energy* **2009**, *83*, 420–431.

42. de Paula, A.C.O.; Ismail, K.A.R. Comprehensive investigation of water film thickness effects on the heat and mass transfer of an inclined solar still. *Desalination* **2021**, *500*, 114895. [CrossRef]

43. Singh, R.G.; Tiwari, G.N. Simulation performance of single slope solar still by using iteration method for convective heat transfer coefficient. *Groundw. Sustain. Dev.* **2020**, *10*, 100287. [CrossRef]
44. Rheinländer, J. Numerical calculation of heat and mass transfer in solar stills. *Sol. Energy* **1982**, *28*, 173–179. [CrossRef]
45. Al-Sulttani, A.O.; Ahsan, A.; Hanoon, A.N.; Rahman, A.; Daud, N.N.N.; Idrus, S. Hourly yield prediction of a double-slope solar still hybrid with rubber scrapers in low-latitude areas based on the particle swarm optimization technique. *Appl. Energy* **2017**, *203*, 280–303. [CrossRef]
46. Gaur, M.K.; Tiwari, G.N. Optimization of number of collectors for integrated PV/T hybrid active solar still. *Appl. Energy* **2010**, *87*, 1763–1772. [CrossRef]
47. Kumar, S.; Tiwari, G.N. Estimation of convective mass transfer in solar distillation systems. *Sol. Energy* **1996**, *57*, 459–464. [CrossRef]
48. Tiwari, G.N.; Tiwari, A.K.; Mahian, O.; Kianifar, A.; Srisomba, R.; Jumpholkul, C.; Thiangtham, P.; Wongwises, S. Solar Distillation Practice for Water Desalination Systems. *J. Therm. Eng.* **2015**, *1*, 287.
49. Elango, C.; Gunasekaran, N.; Sampathkumar, K. Thermal models of solar still—A comprehensive review. *Renew. Sustain. Energy Rev.* **2015**, *47*, 856–911. [CrossRef]
50. Tiwari, G.N.; Shukla, S.K.; Singh, I.P. Computer modeling of passive/active solar stills by using inner glass temperature. *Desalination* **2003**, *154*, 171–185. [CrossRef]
51. Abderachid, T.; Abdenacer, K. Effect of orientation on the performance of a symmetric solar still with a double effect solar still (comparison study). *Desalination* **2013**, *329*, 68–77. [CrossRef]
52. Kennedy, J.; Eberhart, R. Particle swarm optimization. Neural Networks, 1995. In Proceedings of the ICNN'95-International Conference on Neural Networks, Perth, WA, Australia, 27 November–1 December 1995; Volume 4, pp. 1942–1948.
53. Hanoon, A.N.; Jaafar, M.S.; Hejazi, F.; Abdul Aziz, F.N.A. Energy absorption evaluation of reinforced concrete beams under various loading rates based on particle swarm optimization technique. *Eng. Optim.* **2016**, *49*, 1483–1501. [CrossRef]
54. Hanoon, A.N.; Jaafar, M.S.; Hejazi, F.; Aziz, F.N.A.A. Strut-and-tie model for externally bonded CFRP-strengthened reinforced concrete deep beams based on particle swarm optimization algorithm: CFRP debonding and rupture. *Constr. Build. Mater.* **2017**, *147*, 428–447. [CrossRef]
55. Sanikhani, H.; Deo, R.C.; Samui, P.; Kisi, O.; Mert, C.; Mirabbasi, R.; Gavili, S.; Yaseen, Z.M. Survey of different data-intelligent modeling strategies for forecasting air temperature using geographic information as model predictors. *Comput. Electron. Agric.* **2018**, *152*, 242–260. [CrossRef]
56. Hai, T.; Sharafati, A.; Mohammed, A.; Salih, S.Q.; Deo, R.C.; Al-Ansari, N.; Yaseen, Z.M. Global Solar Radiation Estimation and Climatic Variability Analysis Using Extreme Learning Machine Based Predictive Model. *IEEE Access* **2020**, *8*, 12026–12042. [CrossRef]
57. Bokde, N.D.; Yaseen, Z.M.; Andersen, G.B. ForecastTB—An R Package as a Test-Bench for Time Series Forecasting—Application of Wind Speed and Solar Radiation Modeling. *Energies* **2020**, *13*, 2578. [CrossRef]
58. Eberhart, R.; Kennedy, J. A new optimizer using particle swarm theory. In Proceedings of the Sixth International Symposium on Micro Machine and Human Science, MHS'95, Nagoya, Japan, 4–6 October 1995; pp. 39–43.
59. Xie, F.; Wang, Q.; Li, G. Optimization research of FOC based on PSO of induction motors. In Proceedings of the 2012 15th International Conference on Electrical Machines and Systems (ICEMS), Sapporo, Japan, 21–24 October 2012; IEEE: Piscataway, NJ, USA, 2012; pp. 1–4.
60. Adnan, R.M.; Mostafa, R.; Kisi, O.; Yaseen, Z.M.; Shahid, S.; Zounemat-Kermani, M. Improving streamflow prediction using a new hybrid ELM model combined with hybrid particle swarm optimization and grey wolf optimization. *Knowledge-Based Syst.* **2021**, *230*, 107379. [CrossRef]
61. Ehteram, M.; Salih, S.Q.; Yaseen, Z.M. Efficiency evaluation of reverse osmosis desalination plant using hybridized multilayer perceptron with particle swarm optimization. *Environ. Sci. Pollut. Res.* **2020**, *27*, 15278–15291. [CrossRef]
62. Ehteram, M.; Othman, F.B.; Yaseen, Z.M.; Afan, H.A.; Allawi, M.F.; Malek, M.B.A.; Ahmed, A.N.; Shahid, S.; Singh, V.P.; El-Shafie, A. Improving the Muskingum flood routing method using a hybrid of particle swarm optimization and bat algorithm. *Water* **2018**, *10*, 807. [CrossRef]
63. Khare, A.; Rangnekar, S. A review of particle swarm optimization and its applications in solar photovoltaic system. *Appl. Soft Comput.* **2013**, *13*, 2997–3006. [CrossRef]
64. Shi, Y.; Eberhart, R. A modified particle swarm optimizer. In Proceedings of the 1998 IEEE International Conference on Evolutionary Computation Proceedings. IEEE World Congress on Computational Intelligence (Cat. No.98TH8360), Anchorage, AK, USA, 4–9 May 1998.
65. Kulkarni, R.V.; Venayagamoorthy, G.K. Particle Swarm Optimization in Wireless-Sensor Networks: A Brief Survey. *IEEE Trans. Syst. Man, Cybern. Part C Appl. Rev.* **2011**, *41*, 262–267. [CrossRef]
66. Akram, J.; Javed, A.; Khan, S.; Akram, A.; Munawar, H.S.; Ahmad, W. Swarm intelligence based localization in wireless sensor networks. In Proceedings of the 36th Annual ACM Symposium on Applied Computing, New York, NY, USA, 22–26 March 2021.
67. Gandomi, A.H.; Roke, D.A. Assessment of artificial neural network and genetic programming as predictive tools. *Adv. Eng. Softw.* **2015**, *88*, 63–72. [CrossRef]
68. Yaseen, Z.M. An insight into machine learning models era in simulating soil, water bodies and adsorption heavy metals: Review, challenges and solutions. *Chemosphere* **2021**, *277*, 130126. [CrossRef] [PubMed]

69. Golbraikh, A.; Tropsha, A. Beware of q2! *J. Mol. Graph. Model.* **2002**, *20*, 269–276. [CrossRef]
70. Roy, P.P.; Roy, K. On Some Aspects of Variable Selection for Partial Least Squares Regression Models. *QSAR Comb. Sci.* **2008**, *27*, 302–313.
71. Gandomi, A.H.; Alavi, A.H.; Shadmehri, D.M.; Sahab, M.G. An empirical model for shear capacity of RC deep beams using genetic-simulated annealing. *Arch. Civ. Mech. Eng.* **2013**, *13*, 354–369.
72. Frank, I.E.; Todeschini, R. *The Data Analysis Handbook (Vol. 14)*; Elsevier Science Ltd: Amsterdam, The Netherlands, 1994.
73. Smith, G.N. *Probability Statistics Civil Engineering*; Collins: London, UK, 1986.
74. Bland, J.M.; Altman, D.G. Agreement Between Methods of Measurement with Multiple Observations Per Individual. *J. Biopharm. Stat.* **2007**, *17*, 571–582.
75. Natrella, M.G. *Experimental Statistics*; Courier Corporation: Chelmsford, MA, USA, 2013; ISBN 0486154556.
76. Ahmed, S.T. Study of single-effect solar still with an internal condenser. *Sol. Wind Technol.* **1988**, *5*, 637–643. [CrossRef]
77. Cooper, P.I. Solar distillation: State of the art and future prospects. In Proceedings of the Arab International Solar Energy Conference, Kuwait, 2–8 December 1983; Volume 1, pp. 311–330.
78. Durkaieswaran, P.; Murugavel, K.K. Various special designs of single basin passive solar still—A review. *Renew. Sustain. Energy Rev.* **2015**, *49*, 1048–1060.
79. Muftah, A.F.; Alghoul, M.A.; Fudholi, A.; Abdul-Majeed, M.M.; Sopian, K. Factors affecting basin type solar still productivity: A detailed review. *Renew. Sustain. Energy Rev.* **2014**, *32*, 430–447. [CrossRef]
80. Balamurugan, S.; Sundaram, N.S.; Marimuthu, K.P.; Devaraj, J. A Comparative Analysis and Effect of Water Depth on the Performance of Single Slope Basin Type Passive Solar Still Coupled with Flat Plate Collector and Evacuated Tube Collector. *Appl. Mech. Mater.* **2017**, *867*, 195–202. [CrossRef]
81. Sampathkumar, K.; Arjunan, T.V.; Pitchandi, P.; Senthilkumar, P. Active solar distillation—A detailed review. *Renew. Sustain. Energy Rev.* **2010**, *14*, 1503–1526.
82. Al-Hinai, H.; Al-Nassri, M.S.; Jubran, B.A. Effect of climatic, design and operational parameters on the yield of a simple solar still. *Energy Convers. Manag.* **2002**, *43*, 1639–1650.
83. Nafey, A.S.; Abdelkader, M.; Abdelmotalip, A.; Mabrouk, A.A. Parameters affecting solar still productivity. *Energy Convers. Manag.* **2000**, *41*, 1797–1809.
84. Elango, T.; Kalidasa Murugavel, K. The effect of the water depth on the productivity for single and double basin double slope glass solar stills. *Desalination* **2015**, *359*, 82–91. [CrossRef]
85. Bagheri, M.; Bagheri, M.; Gandomi, A.H.; Golbraikh, A. Simple yet accurate prediction method for sublimation enthalpies of organic contaminants using their molecular structure. *Thermochim. Acta* **2012**, *543*, 96–106.
86. Ögelman, H.; Ecevit, A.; Tasdemiroğlu, E. A new method for estimating solar radiation from bright sunshine data. *Sol. Energy* **1984**, *33*, 619–625.
87. Bevington, P.R.; Robinson, D.K.; Bunce, G. Data Reduction and Error Analysis for the Physical Sciences, 2nd ed. *Am. J. Phys.* **1993**, *61*, 766–767.